Towards a Physics Foundation Model

Florian Wiesner
School of Data Science, University of Virginia &
Chemical Process Engineering, RWTH Aachen University
florian.wiesner@rwth-aachen.de

Matthias Wessling
Chemical Process Engineering
RWTH Aachen University
matthias.wessling@avt.rwth-aachen.de

Stephen Baek[*]
School of Data Science
University of Virginia
baek@virginia.edu

Github

Abstract

Foundation models have revolutionized natural language processing through a "*train once, deploy anywhere*" paradigm, where a single pre-trained model adapts to countless downstream tasks without retraining. Access to a **Physics Foundation Model (PFM)** would be transformative—democratizing access to high-fidelity simulations, accelerating scientific discovery, and eliminating the need for specialized solver development. Yet current physics-aware machine learning approaches remain fundamentally limited to single, narrow domains and require retraining for each new system. We present the **General Physics Transformer (GP$_{\text{hy}}$T)**, trained on 1.8 TB of diverse simulation data, that demonstrates foundation model capabilities are achievable for physics. Our key insight is that transformers can learn to infer governing dynamics from context, enabling a single model to simulate fluid-solid interactions, shock waves, thermal convection, and multi-phase dynamics without being told the underlying equations. GP$_{\text{hy}}$T achieves three critical breakthroughs: (1) superior performance across multiple physics domains, outperforming specialized architectures by up to 29x, (2) zero-shot generalization to entirely unseen physical systems through in-context learning, and (3) stable long-term predictions through 50-timestep rollouts. By establishing that a single model can learn generalizable physical principles from data alone, this work opens the path toward a universal PFM that could transform computational science and engineering.

1 Introduction

Over the last few years, massive accumulation of data and large-scale GPU computing have led to extraordinary advancements in language model (LLMs) capabilities (Devlin et al., 2019; Radford et al., 2018; 2019; Raffel et al., 2020; Anil et al., 2023). These frontier foundation models, often exceeding 100 billion parameters, have established a "*train once, deploy anywhere*" paradigm. They generalize to unseen domains and can be prompted to perform diverse tasks—from coding to creative writing—without task-specific finetuning (Brown et al., 2020; Minaee et al., 2025), exhibiting emergent abilities not explicitly programmed (Wei et al., 2022).

We envision a similar paradigm for physics-aware machine learning (PAML), where a single foundation model can simulate a wide range of physical systems, boundary conditions, and initial states. This allows end-users to employ the model for their individual use case without the need for extensive retraining or fine-tuning. However, current state-of-the-art physics models, such as physics-informed neural networks (PINNs) (Raissi et al., 2019), neural operators (Kovachki et al., 2023; Lu et al.,

[*] Corresponding author.

2021), and physics-aware recurrent convolutions (PARC) (Nguyen et al., 2023a; 2024), are fundamentally limited to solving a single, narrowly scoped physical system: While they excel at their specific task, they cannot generalize to new physics or boundary conditions without new or additional training. Even recent multi-physics approaches largely rely on fine-tuning or meta-learning, which still demands new data and training for each application (Penwarden et al., 2023; Cho et al., 2023; McCabe et al., 2024).

The primary barrier to a truly "*train once, deploy anywhere*" Physics Foundation Model (PFM) is the immense diversity of physical phenomena coupled with highly expensive and limited data. A single model intended as a surrogate for computational fluid dynamics, for example, must reconcile the micrometers and milliseconds of microfluidics with the kilometers and hours of weather forecasting. Critically, the same initial state can evolve into vastly different outcomes depending on the governing physical laws. A PFM must therefore either be explicitly provided with a complete system description (e.g. scale, boundary conditions, material properties, governing equations) or infer the dynamics from the given input data itself. As the variety of problems scales, the former becomes impractical and defeats the purpose of a truly general model.

Here, we propose that the path towards PFMs lies in emulating the in-context learning abilities of LLMs (Brown et al., 2020; Agarwal et al., 2024). Instead of being explicitly told the governing equations, a model should infer the underlying dynamics from a "prompt" consisting of a short sequence of prior states. Such a model could adapt its predictions on the fly, enabling a single, unified architecture to tackle a wide array of physical scenarios. This paradigm shift presents fundamental research challenges that we address through the General Physics Transformer (GP$_{\mathrm{hy}}$T) trained on a diverse 1.8 TB corpus of simulation data. With this model, we investigate three critical questions:

Q1: Can a single, large-scale transformer effectively model a wide range of disparate physical systems (e.g., incompressible flow, shock waves, convection) without any explicit, physics-describing features? (Section 4.1)

Q2: Can this foundation model perform zero-shot generalization to new, unseen physical conditions (e.g., new boundary conditions, entirely new physics) by inferring the dynamics from the input alone? (Section 4.2)

Q3: Can GP$_{\mathrm{hy}}$T maintain physical consistency and stability during extended autoregressive rollouts, a characteristic crucial for real-world application? (Section 4.3)

Our results demonstrate that GP$_{\mathrm{hy}}$T not only outperforms specialized architectures on seen tasks but also successfully generalizes to out-of-distribution problems, including producing physically plausible predictions for phenomenon absent from its training data. This work represents a critical step towards creating a "universal physics engine" that could democratize access to high-fidelity simulations and accelerate scientific discovery across disciplines.

2 Related work

Neural Surrogates for Physical Systems Machine learning has emerged as a powerful tool to accelerate the simulation of complex physical systems, which are governed by partial differential equations (PDEs) that lack analytical solutions. The dominant paradigms in this domain are Physics-Informed Neural Networks (PINNs), Neural Operators (NOs) and their combination Physics-informed Neural Operators. PINNs embed the governing PDEs directly into the training process as a soft constraint in the loss function, which enhances data efficiency and physical consistency (Raissi et al., 2019; Karniadakis et al., 2021). This approach has been successfully applied across numerous scientific fields (Faroughi et al., 2024). Neural Operators, in contrast, learn the solution operator mapping from the PDE parameters to the solution space, making them discretization-invariant (Kovachki et al., 2023). Prominent examples include Fourier Neural Operators (FNOs), which perform convolutions in the frequency domain (Li et al., 2020), and DeepONets (Lu et al., 2021). Moreover, combinations of operators with physics-informed loss functions can reduce the data requirements of neural operators (Goswami et al., 2023; Li et al., 2023).

Despite their success, PINNs and NOs are fundamentally specialized solvers. They are typically designed and trained for a single, well-defined physical system and struggle to generalize to new governing equations, boundary conditions, or complex multi-physics phenomena without transfer learning (Goswami et al., 2022; 2020) or full retraining. This inherent specialization prevents them from serving as true "foundational" models in the way that large language models (LLMs) do for natural language tasks.

Towards Foundational Models for Science The concept of a large-scale foundation model pretrained on extensive, diverse data has begun to permeate scientific disciplines. This has led to two distinct categories of models. The first involves language-based models fine-tuned on scientific corpora, such as AstroLLaMA for astronomy (Nguyen et al., 2023b) or specialized models for interpreting medical records (Jiang et al., 2023). The second category comprises models that operate directly on quantitative scientific data such as velocity or temperature fields. Notable examples are models for molecular structures (Chithrananda et al., 2020), climate forecasts (Nguyen et al., 2023c), or aquatic science (Yu et al., 2025). Regardless of methodology, any foundation model must either be capable generalizing to unseen data or finetuned for new tasks (Choi et al., 2025).

In physics, the pursuit of foundation models has largely focused on enhancing the generalization of neural surrogates. Researchers have explored meta-learning (Penwarden et al., 2023) and transfer learning (Subramanian et al., 2023; Goswami et al., 2022) to adapt pretrained models to new PDE systems with fewer data samples. Recently, multi-tasks models trained on multiple physical systems were explored McCabe et al. (2024). However, while both groups demonstrated superior accuracy compared to single-physics models, both opted for finetuning to unseen tasks. These efforts represent important progress, but they still fall short of the “*train once, deploy anywhere*” paradigm that we envision.

Transformers for Spatiotemporal Modeling The architectural backbone of most modern foundation models is the Transformer (Vaswani et al., 2017), whose self-attention mechanism has proven exceptionally effective at capturing long-range dependencies in sequential data. Originally developed for language, this architecture was successfully adapted for computer vision in the Vision Transformer (ViT) (Dosovitskiy et al., 2020). By treating an image as a sequence of patches, ViTs achieved state-of-the-art performance with sufficient data provided (Khan et al., 2023). This concept was further extended to video by creating spatiotemporal "tubelet" tokens (Arnab et al., 2021), enabling transformers to model dynamic visual data. The power of transformers also extends to generative tasks. Using vector quantization, auto-regressive transformer models can operate on a discrete latent space of visual tokens (Esser et al., 2021; Chang et al., 2022; Ramesh et al., 2021).

3 General Physics Transformer

3.1 Architecture

Due to data scarcity, today’s physics models must incorporate inductive biases for optimal performance. However, the diversity of multiple physical systems restricts such choices. The General Physics Transformer (GP$_{\text{hy}}$T) is designed as a hybrid model that integrates a deep learning component within a classic numerical methods framework. As illustrated in Figure 1a, the core of our architecture is a Transformer-based neural differentiator that learns the temporal dynamics of a system, coupled with a standard numerical integrator that extrapolates the system’s future state. This approach, inspired by Neural ODEs (Chen et al., 2018) and previous work of Nguyen et al. (2024), allows the model to predict the evolution of diverse physical systems governed by partial differential equations (PDEs).

Neural differentiator The neural differentiator (blue dashed box) models the partial derivative ($\frac{\partial X}{\partial t}$) of the physical state with respect to time. X is composed for multiple physical fields (channels), such as pressure, temperature, and velocity. To allow for in-context learning, the differentiator receives multiple time snapshots ($X_{t_i - n}, ..., X_{t_i}$) of the physical state. The sample is then tokenized by a single linear transformation across spatial and temporal dimensions, yielding non-overlapping spatiotemporal (tubelet (Arnab et al., 2021)) patches. The size of these patches control the number of spatial and temporal pixels encoded in each token. Absolute positional encodings are added to the patches. The spatiotemporal transformer consists of multiple transformer layers with layer norms and attention across all time and space dimensions, illustrated in Figure 1b. We chose this unified attention mechanism over more computationally efficient factorized approaches to ensure maximum expressivity, allowing the model to capture complex, non-separable phenomena like turbulence and shockwave interactions. Finally, a linear transformation (detokenizer) reverts the spatiotemporal patches into the input space.

To provide the model with explicit local information, we compute the first-order spatial (dx, dy) and temporal (dt) derivatives of the input fields using central differences. These computed derivatives are concatenated with the original fields along the channel dimension, enriching the input for the neural differentiator. This technique is particularly effective for resolving phenomena with sharp gradients (Cheng et al., 2024).

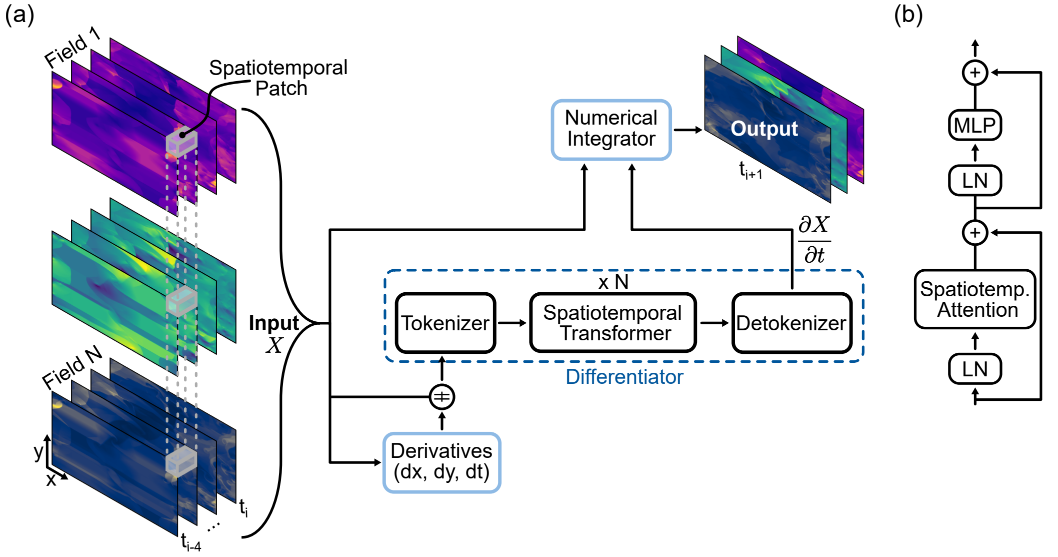

Figure 1: (a) General architecture of GP$_{\text{hy}}$T. A 4D-stack of physical quantities (time, height, width, fields) serves as input X. The numerically computed derivatives of each field are concatenated to the input. The differentiator (linear tokenizer, spatiotemporal transformer, linear detokenizer) provides the partial derivative of X wrt. time. Finally, a numerical integrator computes the next timestep of each field given $\frac{\partial X}{\partial t}$ and X. (b) Architecture of a single transformer layer, consisting of layer norms (LN), spatiotemporal attention, and multilayer perceptron (MLP).

Numerical Integrator With the learned time derivative, we can predict the next state of the system, $X_{t_{i+1}}$, using a numerical integration step. The general form of the integration is:

$$X_{t_{i+1}} = f\left(X_{t_i}, \left.\frac{\partial X}{\partial t}\right|_{t_i}, \Delta t\right) \tag{1}$$

In this study, we choose the first-order Forward Euler method. An ablation study in Appendix 6.4 showed that higher-order integrators like Runge–Kutta 4 provided no significant accuracy benefit for our framework, making Forward Euler the most computationally efficient choice.

3.2 Datasets

To train a model capable of learning general physical principles, we curated a large and diverse corpus of simulation data, comprising eight distinct datasets listed in Table 1. The combined dataset contains over 2.4 million simulation snapshots, totaling 1.8 TB of data. Our data is sourced from both the publicly available "The Well" benchmark (Ohana et al., 2024) and our own custom simulations, described in detail in Appendix 6.6.

The three datasets from The Well cover a range of fundamental physics, including incompressible (Shear flow) and compressible (Euler) fluid dynamics, and thermal convection (Rayleigh–Bénard). However, these systems largely lack the solid boundaries and complex geometries prevalent in engineering applications. To address this, we generated four additional datasets featuring flows around rigid obstacles, Rayleigh–Bénard with additional obstacles, heat exchange with solid elements (Thermal Flow), and multi-phase dynamics in porous media. These additions introduce critical physical behaviors, such as boundary layer formation, vortex shedding, pressure-driven instabilities, as well as varying physical scales, significantly expanding the diversity of the training data.

Table 1: Dataset overview. Each trajectory has different initial conditions / randomized geometry and contains the given number of timesteps. Unique samples are all possible combinations of 4 input and 1 output snapshots sampled for time-increments of 1-8 and random axis flips.

Dataset	Trajectories	Timesteps	Snapshots	Unique samples	Origin
Shear flow	1120	200	224,000	6,522,880	The Well
Rayleigh–Bénard	1750	200	350,000	10,192,000	The Well
Euler	5000	100	500,000	13,120,000	The Well
Obstacle flow	1266	481	608,946	18,756,856	Own
Thermal flow	354	481	170,274	5,244,864	Own
Rayleigh–Bénard 2	228	1001	228,228	7,171,968	Own
Twophase flow	816	401	327,216	10,000,896	Own
Sum			**2,408,664**	**71,009,464**	

A core objective of this work is to train a model that can generalize by inferring the underlying physics from context. To facilitate this, we implemented two crucial data augmentation strategies:

- **Variable Time Increments:** Each simulation trajectory is sub-sampled using multiple time-step increments (Δt). This forces the model to learn dynamics that are invariant to the sampling frequency. For any given input, the model must infer the temporal scale from the dynamics presented in the prompt, as a single time step could represent milliseconds in one context and minutes in another.
- **Per-Dataset Normalization:** The physical phenomena in our corpus span vastly different scales, from micrometer-sized pores in two-phase flow to large-scale convective cells. To handle this, we normalize each dataset independently. This preserves the relative physical quantities within a single simulation while compelling the model to infer the absolute magnitudes and spatial scales of a new system purely from the context provided by the input snapshots.

By training on this varied data, $\text{GP}_{\text{hy}}\text{T}$ is explicitly pushed to develop in-context learning abilities, rather than memorizing the characteristics of a single, fixed physical system.

4 Results

4.1 Multi-physics learning

To answer our first research question **Q1**—whether a single model can effectively learn to represent numerous, disparate physical systems—we evaluated $\text{GP}_{\text{hy}}\text{T}$'s single-step prediction accuracy across our entire multi-physics test set. We benchmarked against two established architectures: the Fourier Neural Operator (FNO) (Kovachki et al., 2023), and a standard UNet, a widely-adopted baseline for spatiotemporal prediction tasks. All models were trained identically on 4 initial frames to predict the subsequent frame, ensuring a fair comparison.

Figure 2 presents the average and median mean squared error (MSE) across all test sets. $\text{GP}_{\text{hy}}\text{T}$ demonstrates substantial performance gains in average MSE and achievs a 5× reduction in median MSE compared to UNet and a 29× reduction compared to FNO at equivalent model sizes (size M). Detailed per-dataset losses are provided in SI section 6.2. Remarkably, even our smallest variant ($\text{GP}_{\text{hy}}\text{T}$) with only 10% of the parameters outperforms the full-sized FNO and UNet when comparing median MSE. This efficiency gain suggests that the spatiotemporal attention mechanism captures cross-scale physical interactions more effectively than traditional convolutional or neural operator approaches. Furthermore, $\text{GP}_{\text{hy}}\text{T}$ exhibits favorable scaling properties with performance gains from the S to XL variants, indicating potential for further improvements with increased model capacity.

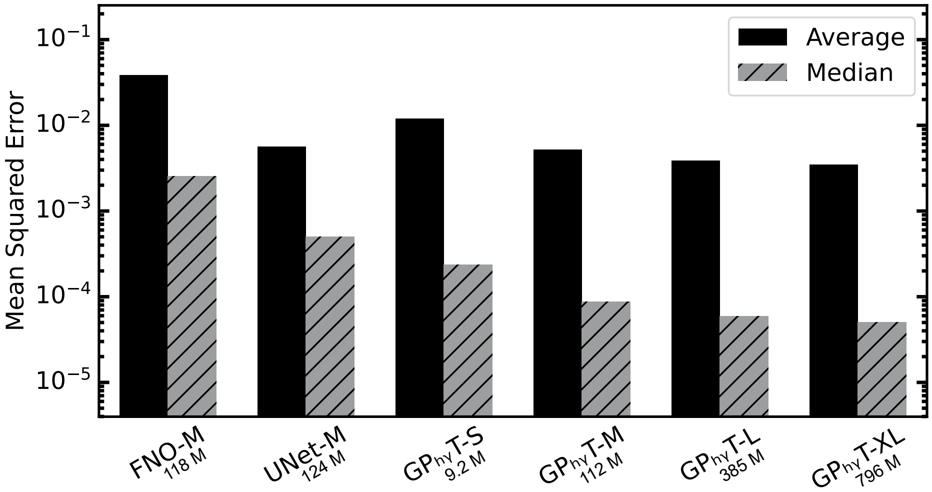

Figure 2: Average and median mean squared error (MSE) across all test sets for each model (lower is better). Number of parameters (in million) are given below model names.

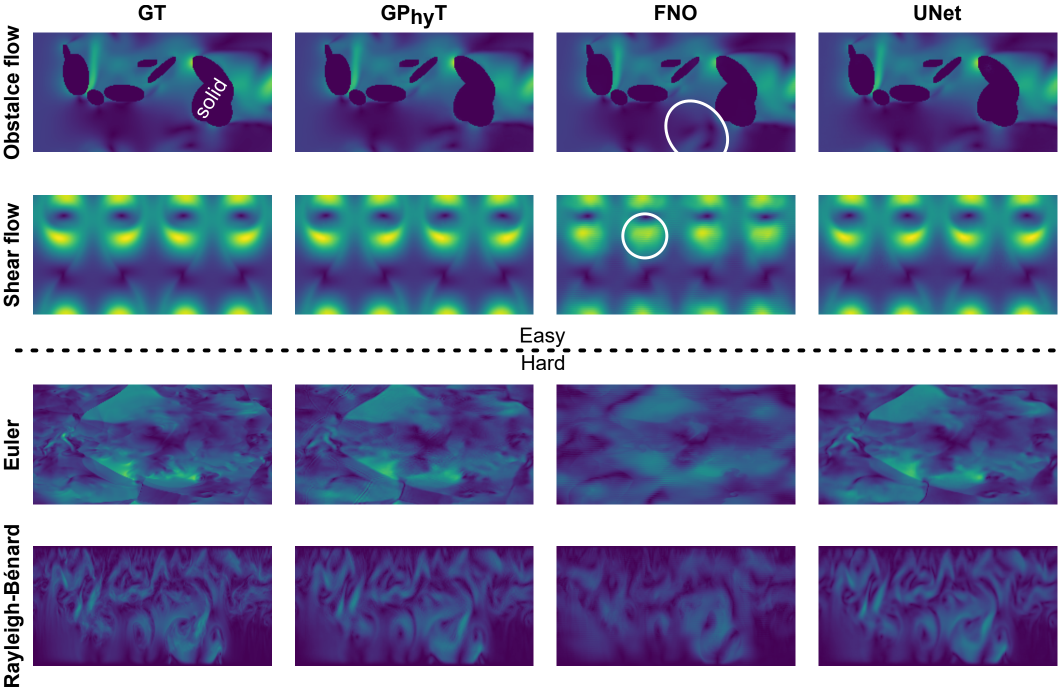

Figure 3: Next timestep prediction (velocity magnitude) of GP$_{\mathrm{hy}}$T, Unet, and FNO in their M-variant against ground truth (GT). Top row: Incompressible flow with periodic boundary conditions and $\Delta t = 8$. 2nd row: Shear flow ($\Delta t = 4$). 3rd row: Euler shock waves with periodic boundary conditions ($\Delta t = 4$). 4th row: Rayleigh–Bénard convection ($\Delta t = 4$). The results can be best viewed on a high-definition digital monitor.

Figure 3 provides qualitative comparisons across representative physical systems, categorized by complexity. For smooth systems (top two rows: obstacle flow and shear flow), GP$_{\mathrm{hy}}$T and UNet precisely capture fine-scale vortical structures and boundary layer dynamics, while the FNO struggles with spatial localization. For more challenging systems featuring discontinuities and chaotic dynamics (bottom two rows: Euler shocks and Rayleigh–Bénard convection), the performance gap widens dramatically. GP$_{\mathrm{hy}}$T maintains sharp shock fronts and accurately tracks convective plumes, while the

FNO fails to resolve these critical features, producing overly smoothed predictions that miss essential physical phenomena. The UNet produces reasonable approximations but exhibits some diffusion of sharp features. These results suggest that the GP$_{\text{hy}}$T architecture, with its ability to dynamically attend to relevant spatiotemporal features, is inherently better suited as a Physics Foundation Model than FNO and UNet.

4.2 Zero-shot in-context learning

The defining characteristic of a true foundation model is its ability to adapt to new tasks without additional training—a capability that fundamentally distinguishes them from traditional specialized models. In language models, this emerges through in-context learning, where models leverage prompts to perform tasks never explicitly seen during training (Brown et al., 2020). To investigate our research question **Q2**, whether GP$_{\text{hy}}$T exhibits similar emergent capabilities for physics, we designed increasingly challenging generalization experiments: First, we evaluated the model on systems with modified boundary conditions completely absent from the training data. Second, we pushed the boundaries further by presenting entirely novel physical phenomena, including supersonic flows and turbulent radiative layers never encountered during training. These experiments probe whether the model has learned transferable physical principles rather than memorizing dataset-specific patterns.

Table 2: Average MSE for in-context learning tasks. The model is evaluated on systems with new boundary conditions and entirely new physics, with known systems provided as a baseline.

Dataset	**Variant**	**Zero-shot MSE**
Obstacle flow		
Symmetric	Known	2.97×10^{-4}
Periodic	Known	5.32×10^{-4}
Open	**New**	8.01×10^{-3}
Euler		
Periodic	Known	8.92×10^{-3}
Open	**New**	9.09×10^{-3}
Turbulent layer	**New**	2.05×10^{-1}
Supersonic	**New**	1.40×10^{-1}

The quantitative results are summarized in Table 2, with qualitative examples shown in Figure 4 and Section 6.8 in the Appendix. For incompressible flow around obstacles, introducing a new "open" boundary condition, where mass is not conserved, results in an average MSE nearly identical to the MSE achieved on the "known" symmetric system. Even more striking is the result for the chaotic Euler system, where the open boundary variant achieves the same accuracy compared to the known periodic system. Thus, GP$_{\text{hy}}$T successfully infers new boundary conditions from the prompt without the need for finetuning.

The most challenging tests are two completely new physical systems: Supersonic flow around an obstacle and a turbulent radiative layer. Here, the MSE is significantly higher than in the known systems, emphasizing the significant challenge. Yet, Figure 4 shows that GP$_{\text{hy}}$T still captures the essential dynamics, correctly forming a bow shock and the overall flow field for the supersonic flow. Similarly, the general turbulent features are present in the turbulent radiative layer. Naturally, finetuning the model on the new systems as done in previous studies McCabe et al. (2024); Subramanian et al. (2023) will yield even more accurate predictions, however, the ability to extrapolate and produce a physically plausible result for entirely new physics, even with reduced accuracy, is a powerful demonstration of emergent generalization.

4.3 Long-range Prediction

As stated in research question **Q3**, the true utility of any physics surrogate model is measured by its ability to maintain stability and accuracy over extended temporal horizons. This task is exceptionally challenging, as it requires the model to generate a full trajectory from an initial state, with prediction

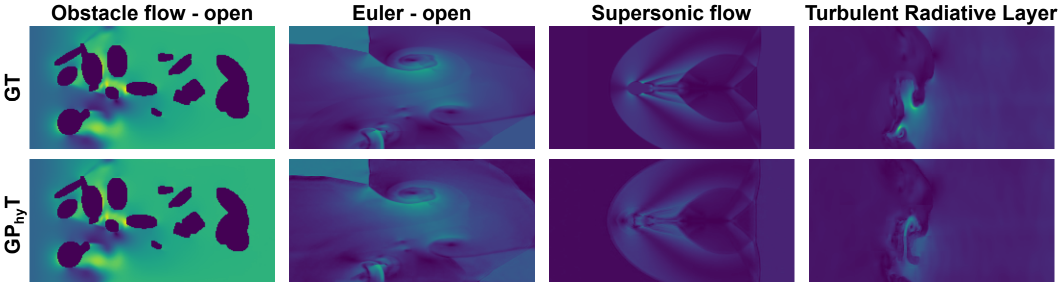

Figure 4: Qualitative results for in-context learning. $GP_{hy}T$ accurately predicts the next state for an incompressible flow and Euler flow with unseen open boundary conditions (1st and 2nd column). For the completely new physics of supersonic flow (3rd column), it successfully captures the formation of a bow shock wave, demonstrating strong zero-shot generalization. For the turbulent radiative layer (4th column), general turbulent features are present while finegrained details are missing. The results can be best viewed on a high-definition digital monitor.

errors from each step accumulating over time. It is a critical test of a model's physical consistency and a common failure point that is often omitted in literature.

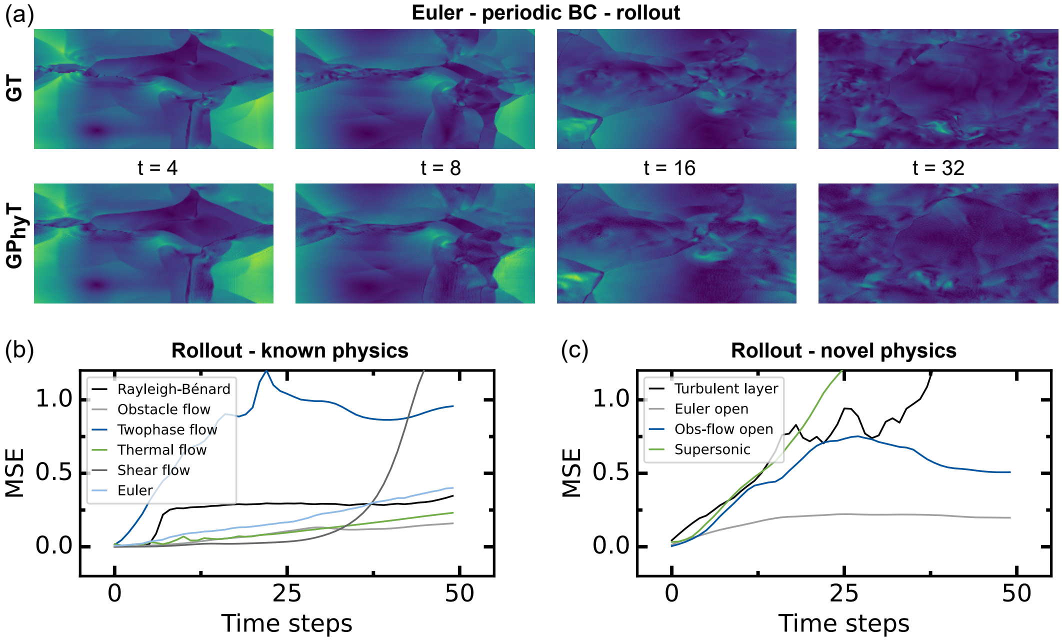

Figure 5: (a) Autoregressive rollout prediction for velocity magnitude of $GP_{hy}T$-XL on the Euler shockwaves with periodic boundary conditions. (b) Average mean squared error (MSE) over 50 time steps for all known physical systems. (c) Average MSE over 50 time steps for the novel unseen physical systems. The results can be best viewed on a high-definition digital monitor.

Figure 5a) illustrates a 50-timestep autoregressive rollout for an Euler shockwave. In the initial phase (t=16), $GP_{hy}T$-XL maintains high fidelity, accurately capturing the intricate vortex structures and shock fronts of the ground truth. As the rollout progresses, error accumulation becomes visible as a loss of high-frequency detail (t=32). However, the model successfully preserves the global dynamics and physical plausibility of the flow; the large-scale structures and boundary interactions remain stable and coherent. The quantitative evaluation across the known physical systems is shown in Figure 5b). For most physics, $GP_{hy}T$'s exhibit near-linear error accumulation over 25 timesteps. Exceptions are twophase flow, where changes can occur extremely abrupt, and shear flow, where a chaotic initial system converges to a quasi-static solution.

Extension to out-of-distribution systems (Figure 5c) provides further insight into the model's generalization mechanisms. Systems with modified boundary conditions maintain error trajectories comparable to their training counterparts. Specifically, Euler with open boundaries tracks the periodic case almost identically, suggesting the model has disentangled bulk dynamics from boundary effects. For entirely novel physics error growth rates are higher, highlighting the need for even more accurate and stable physics foundation models.

5 Conclusion

We have demonstrated that a single transformer-based model can effectively learn and predict the dynamics of diverse physical systems without explicit physics-specific features, marking a significant step toward true Physics Foundation Models. $\mathrm{GP_{hy}T}$ not only outperforms specialized architectures on known physics by up to an order of magnitude but, more importantly, exhibits emergent in-context learning capabilities—inferring new boundary conditions and even entirely novel physical phenomena from input prompts alone. This "*train once, deploy anywhere*" capability, previously exclusive to language models, opens new possibilities for physics simulation. Our hybrid architecture, combining a transformer-based neural differentiator with numerical integration, proves that the attention mechanism can capture complex spatiotemporal dependencies across vastly different scales. The model's ability to maintain physical consistency through 50-timestep rollouts, while not yet matching numerical solvers, demonstrates that learned representations can encode generalizable physical principles rather than merely memorizing dataset-specific patterns. The path toward a comprehensive Physics Foundation Model requires addressing current limitations: extending to 3D systems, incorporating diverse physical domains beyond fluid dynamics, and achieving variable-resolution capabilities. Most critically, improving long-term stability will be essential for practical engineering applications. Nevertheless, $\mathrm{GP_{hy}T}$ establishes that the foundation model paradigm, i.e. a single pre-trained model adapting to novel tasks through context alone, is achievable for physics. As we scale both model capacity and training data diversity, we anticipate further emergent capabilities that could fundamentally transform how we approach computational physics, making high-fidelity simulations accessible to researchers and engineers without the traditional barriers of specialized solver development or extensive computational resources.

Acknowledgments

F.W acknowledges financial support from the German Federal Ministry of Research, Technology and Space (BMFTR project "PrometH2eus", FKZ 03HY105A). M.W. acknowledges DFG funding through the Gottfried Wilhelm Leibniz Award 2019 (WE 4678/12-1). S.B. acknowledges financial support from the National Science Foundation (Award No. DMREF-2203580). The authors acknowledge Research Computing at the University of Virginia for providing computational resources that have contributed to the results reported within this paper. Additional computational resources were provided by the German AI Service Center WestAI. The authors acknowledge the use of LLMs for improved grammar and wording in the manuscript. Furthermore, they acknowledge the use of coding agents (e.g. Claude code / Cursor) to generate boilerplate code and to draft unit tests. The views and conclusions of this work are those of the authors only.

Reproducibility statement

All training, evaluation and plotting code will be published. Furthermore, model checkpoints will be released on Hugging Face. Finally, the datasets which are not available on The Well will be avaiable to download.

References

Rishabh Agarwal, Avi Singh, Lei M. Zhang, Bernd Bohnet, Luis Rosias, Stephanie C. Y. Chan, Biao Zhang, Aleksandra Faust, and Hugo Larochelle. Many-shot In-Context Learning. In *ICML 2024*, June 2024. doi: 10.48550/arXiv.2404.11018.

Rohan Anil, Andrew M. Dai, Orhan Firat, Melvin Johnson, Dmitry Lepikhin, Alexandre Passos, Siamak Shakeri, Emanuel Taropa, Paige Bailey, Zhifeng Chen, Eric Chu, Jonathan H. Clark, Laurent El Shafey, Yanping Huang, Kathy Meier-Hellstern, Gaurav Mishra, Erica Moreira, Mark Omernick, Kevin Robinson, Sebastian Ruder, Yi Tay, Kefan Xiao, Yuanzhong Xu, Yujing Zhang, Gustavo Hernandez Abrego, Junwhan Ahn, Jacob Austin, Paul Barham, Jan Botha, James Bradbury, Siddhartha Brahma, Kevin Brooks, Michele Catasta, Yong Cheng, Colin Cherry, Christopher A. Choquette-Choo, Aakanksha Chowdhery, Clément Crepy, Shachi Dave, Mostafa Dehghani, Sunipa Dev, Jacob Devlin, Mark Díaz, Nan Du, Ethan Dyer, Vlad Feinberg, Fangxiaoyu Feng, Vlad Fienber, Markus Freitag, Xavier Garcia, Sebastian Gehrmann, Lucas Gonzalez, Guy Gur-Ari, Steven Hand, Hadi Hashemi, Le Hou, Joshua Howland, Andrea Hu, Jeffrey Hui, Jeremy Hurwitz, Michael Isard, Abe Ittycheriah, Matthew Jagielski, Wenhao Jia, Kathleen Kenealy, Maxim Krikun, Sneha Kudugunta, Chang Lan, Katherine Lee, Benjamin Lee, Eric Li, Music Li, Wei Li, YaGuang Li, Jian Li, Hyeontaek Lim, Hanzhao Lin, Zhongtao Liu, Frederick Liu, Marcello Maggioni, Aroma Mahendru, Joshua Maynez, Vedant Misra, Maysam Moussalem, Zachary Nado, John Nham, Eric Ni, Andrew Nystrom, Alicia Parrish, Marie Pellat, Martin Polacek, Alex Polozov, Reiner Pope, Siyuan Qiao, Emily Reif, Bryan Richter, Parker Riley, Alex Castro Ros, Aurko Roy, Brennan Saeta, Rajkumar Samuel, Renee Shelby, Ambrose Slone, Daniel Smilkov, David R. So, Daniel Sohn, Simon Tokumine, Dasha Valter, Vijay Vasudevan, Kiran Vodrahalli, Xuezhi Wang, Pidong Wang, Zirui Wang, Tao Wang, John Wieting, Yuhuai Wu, Kelvin Xu, Yunhan Xu, Linting Xue, Pengcheng Yin, Jiahui Yu, Qiao Zhang, Steven Zheng, Ce Zheng, Weikang Zhou, Denny Zhou, Slav Petrov, and Yonghui Wu. PaLM 2 Technical Report. September 2023. doi: 10.48550/arXiv.2305.10403.

Anurag Arnab, Mostafa Dehghani, Georg Heigold, Chen Sun, Mario Lučić, and Cordelia Schmid. ViViT: A Video Vision Transformer. In *2021 IEEE/CVF International Conference on Computer Vision (ICCV)*, pp. 6816–6826, October 2021. doi: 10.1109/ICCV48922.2021.00676.

Tom Brown, Benjamin Mann, Nick Ryder, Melanie Subbiah, Jared D Kaplan, Prafulla Dhariwal, Arvind Neelakantan, Pranav Shyam, Girish Sastry, Amanda Askell, Sandhini Agarwal, Ariel Herbert-Voss, Gretchen Krueger, Tom Henighan, Rewon Child, Aditya Ramesh, Daniel Ziegler, Jeffrey Wu, Clemens Winter, Chris Hesse, Mark Chen, Eric Sigler, Mateusz Litwin, Scott Gray, Benjamin Chess, Jack Clark, Christopher Berner, Sam McCandlish, Alec Radford, Ilya Sutskever, and Dario Amodei. Language Models are Few-Shot Learners. In *Advances in Neural Information Processing Systems*, volume 33, pp. 1877–1901. Curran Associates, Inc., 2020.

Huiwen Chang, Han Zhang, Lu Jiang, Ce Liu, and William T. Freeman. MaskGIT: Masked Generative Image Transformer. In *2022 IEEE/CVF Conference on Computer Vision and Pattern Recognition (CVPR)*, pp. 11305–11315, New Orleans, LA, USA, June 2022. IEEE. ISBN 978-1-6654-6946-3. doi: 10.1109/CVPR52688.2022.01103.

Ricky T. Q. Chen, Yulia Rubanova, Jesse Bettencourt, and David K Duvenaud. Neural Ordinary Differential Equations. In *Advances in Neural Information Processing Systems*, volume 31. Curran Associates, Inc., 2018. doi: 10.48550/arXiv.1806.07366.

Xinlun Cheng, Phong C.H. Nguyen, Pradeep K. Seshadri, Mayank Verma, Zoë J. Gray, Jack T. Beerman, H.S. Udaykumar, and Stephen S. Baek. Physics-aware recurrent convolutional neural networks for modeling multiphase compressible flows. *International Journal of Multiphase Flow*, 177:104877, July 2024. ISSN 03019322. doi: 10.1016/j.ijmultiphaseflow.2024.104877.

Seyone Chithrananda, Gabriel Grand, and Bharath Ramsundar. ChemBERTa: Large-Scale Self-Supervised Pretraining for Molecular Property Prediction. October 2020. doi: 10.48550/arXiv.2010.09885.

Woojin Cho, Kookjin Lee, Donsub Rim, and Noseong Park. Hypernetwork-based Meta-Learning for Low-Rank Physics-Informed Neural Networks. In *Thirty-Seventh Conference on Neural Information Processing Systems*, November 2023. doi: 10.48550/arXiv.2310.09528.

Youngsoo Choi, Siu Wun Cheung, Youngkyu Kim, Ping-Hsuan Tsai, Alejandro N. Diaz, Ivan Zanardi, Seung Whan Chung, Dylan Matthew Copeland, Coleman Kendrick, William Anderson, Traian Iliescu, and Matthias Heinkenschloss. Defining Foundation Models for Computational Science: A Call for Clarity and Rigor, May 2025.

Jacob Devlin, Ming-Wei Chang, Kenton Lee, and Kristina Toutanova. BERT: Pre-training of Deep Bidirectional Transformers for Language Understanding. In Jill Burstein, Christy Doran, and

Thamar Solorio (eds.), *Proceedings of the 2019 Conference of the North American Chapter of the Association for Computational Linguistics: Human Language Technologies, Volume 1 (Long and Short Papers)*, pp. 4171–4186, Minneapolis, Minnesota, June 2019. Association for Computational Linguistics. doi: 10.18653/v1/N19-1423.

Alexey Dosovitskiy, Lucas Beyer, Alexander Kolesnikov, Dirk Weissenborn, Xiaohua Zhai, Thomas Unterthiner, Mostafa Dehghani, Matthias Minderer, Georg Heigold, Sylvain Gelly, Jakob Uszkoreit, and Neil Houlsby. An Image is Worth 16x16 Words: Transformers for Image Recognition at Scale. In *International Conference on Learning Representations*, October 2020. doi: 10.48550/arXiv.2010.11929.

Patrick Esser, Robin Rombach, and Björn Ommer. Taming Transformers for High-Resolution Image Synthesis. In *2021 IEEE/CVF Conference on Computer Vision and Pattern Recognition (CVPR)*, pp. 12868–12878. IEEE Computer Society, June 2021. ISBN 978-1-6654-4509-2. doi: 10.1109/CVPR46437.2021.01268.

Salah A. Faroughi, Nikhil M. Pawar, Célio Fernandes, Maziar Raissi, Subasish Das, Nima K. Kalantari, and Seyed Kourosh Mahjour. Physics-Guided, Physics-Informed, and Physics-Encoded Neural Networks and Operators in Scientific Computing: Fluid and Solid Mechanics. *Journal of Computing and Information Science in Engineering*, 24(040802), January 2024. ISSN 1530-9827. doi: 10.1115/1.4064449.

Somdatta Goswami, Cosmin Anitescu, Souvik Chakraborty, and Timon Rabczuk. Transfer learning enhanced physics informed neural network for phase-field modeling of fracture. *Theoretical and Applied Fracture Mechanics*, 106:102447, April 2020. ISSN 0167-8442. doi: 10.1016/j.tafmec.2019.102447.

Somdatta Goswami, Katiana Kontolati, Michael D. Shields, and George Em Karniadakis. Deep transfer operator learning for partial differential equations under conditional shift. *Nature Machine Intelligence*, 4(12):1155–1164, December 2022. ISSN 2522-5839. doi: 10.1038/s42256-022-00569-2.

Somdatta Goswami, Aniruddha Bora, Yue Yu, and George Em Karniadakis. Physics-Informed Deep Neural Operator Networks. In Timon Rabczuk and Klaus-Jürgen Bathe (eds.), *Machine Learning in Modeling and Simulation: Methods and Applications*, pp. 219–254. Springer International Publishing, Cham, 2023. ISBN 978-3-031-36644-4. doi: 10.1007/978-3-031-36644-4_6.

Gao Huang, Yu Sun, Zhuang Liu, Daniel Sedra, and Kilian Q. Weinberger. Deep Networks with Stochastic Depth. In Bastian Leibe, Jiri Matas, Nicu Sebe, and Max Welling (eds.), *Computer Vision – ECCV 2016*, pp. 646–661, Cham, 2016. Springer International Publishing. ISBN 978-3-319-46493-0. doi: 10.1007/978-3-319-46493-0_39.

Lavender Yao Jiang, Xujin Chris Liu, Nima Pour Nejatian, Mustafa Nasir-Moin, Duo Wang, Anas Abidin, Kevin Eaton, Howard Antony Riina, Ilya Laufer, Paawan Punjabi, Madeline Miceli, Nora C. Kim, Cordelia Orillac, Zane Schnurman, Christopher Livia, Hannah Weiss, David Kurland, Sean Neifert, Yosef Dastagirzada, Douglas Kondziolka, Alexander T. M. Cheung, Grace Yang, Ming Cao, Mona Flores, Anthony B. Costa, Yindalon Aphinyanaphongs, Kyunghyun Cho, and Eric Karl Oermann. Health system-scale language models are all-purpose prediction engines. *Nature*, 619 (7969):357–362, 2023. ISSN 0028-0836. doi: 10.1038/s41586-023-06160-y.

George Em Karniadakis, Ioannis G. Kevrekidis, Lu Lu, Paris Perdikaris, Sifan Wang, and Liu Yang. Physics-informed machine learning. *Nature Reviews Physics*, 3(6):422–440, June 2021. ISSN 2522-5820. doi: 10.1038/s42254-021-00314-5.

Asifullah Khan, Zunaira Rauf, Anabia Sohail, Abdul Rehman Khan, Hifsa Asif, Aqsa Asif, and Umair Farooq. A survey of the vision transformers and their CNN-transformer based variants. *Artificial Intelligence Review*, 56(3):2917–2970, December 2023. ISSN 1573-7462. doi: 10.1007/s10462-023-10595-0.

Jean Kossaifi, Nikola Kovachki, Zongyi Li, David Pitt, Miguel Liu-Schiaffini, Valentin Duruisseaux, Robert Joseph George, Boris Bonev, Kamyar Azizzadenesheli, Julius Berner, and Anima Anandkumar. A Library for Learning Neural Operators, June 2025.

Nikola Kovachki, Zongyi Li, Burigede Liu, Kamyar Azizzadenesheli, Kaushik Bhattacharya, Andrew Stuart, and Anima Anandkumar. Neural Operator: Learning Maps Between Function Spaces With Applications to PDEs. *Journal of Machine Learning Research*, 24(89):1–97, 2023. ISSN 1533-7928. doi: 10.5555/3648699.3648788.

Zongyi Li, Nikola Borislavov Kovachki, Kamyar Azizzadenesheli, Burigede Liu, Kaushik Bhattacharya, Andrew Stuart, and Anima Anandkumar. Fourier Neural Operator for Parametric Partial Differential Equations. In *International Conference on Learning Representations*, October 2020. doi: 10.48550/arXiv.2010.08895.

Zongyi Li, Hongkai Zheng, Nikola Kovachki, David Jin, Haoxuan Chen, Burigede Liu, Kamyar Azizzadenesheli, and Anima Anandkumar. Physics-Informed Neural Operator for Learning Partial Differential Equations, July 2023.

Lu Lu, Pengzhan Jin, and George Em Karniadakis. DeepONet: Learning nonlinear operators for identifying differential equations based on the universal approximation theorem of operators. *Nature Machine Intelligence*, 3(3):218–229, March 2021. ISSN 2522-5839. doi: 10.1038/s42256-021-00302-5.

Michael McCabe, Bruno Régaldo-Saint Blancard, Liam Parker, Ruben Ohana, Miles Cranmer, Alberto Bietti, Michael Eickenberg, Siavash Golkar, Geraud Krawezik, Francois Lanusse, Mariel Pettee, Tiberiu Tesileanu, Kyunghyun Cho, and Shirley Ho. Multiple physics pretraining for spatiotemporal surrogate models. In A. Globerson, L. Mackey, D. Belgrave, A. Fan, U. Paquet, J. Tomczak, and C. Zhang (eds.), *Advances in Neural Information Processing Systems*, volume 37, pp. 119301–119335. Curran Associates, Inc., 2024. doi: 10.48550/arXiv.2310.02994.

Shervin Minaee, Tomas Mikolov, Narjes Nikzad, Meysam Chenaghlu, Richard Socher, Xavier Amatriain, and Jianfeng Gao. Large Language Models: A Survey, March 2025.

Phong C. H. Nguyen, Yen-Thi Nguyen, Joseph B. Choi, Pradeep K. Seshadri, H. S. Udaykumar, and Stephen S. Baek. PARC: Physics-aware recurrent convolutional neural networks to assimilate meso scale reactive mechanics of energetic materials. *Science Advances*, 9(17):eadd6868, April 2023a. ISSN 2375-2548. doi: 10.1126/sciadv.add6868.

Phong C. H. Nguyen, Xinlun Cheng, Shahab Azarfar, Pradeep Seshadri, Yen T. Nguyen, Munho Kim, Sanghun Choi, H. S. Udaykumar, and Stephen Baek. PARCv2: Physics-aware Recurrent Convolutional Neural Networks for Spatiotemporal Dynamics Modeling. In *Proceedings of the 41st International Conference on Machine Learning*, pp. 37649–37666. PMLR, July 2024.

Tuan Dung Nguyen, Yuan-Sen Ting, Ioana Ciuca, Charles O'Neill, Ze-Chang Sun, Maja Jabłońska, Sandor Kruk, Ernest Perkowski, Jack Miller, Jason Jason Jingsh Li, Josh Peek, Kartheik Iyer, Tomasz Rozanski, Pranav Khetarpal, Sharaf Zaman, David Brodrick, Sergio J. Rodriguez Mendez, Thang Bui, Alyssa Goodman, Alberto Accomazzi, Jill Naiman, Jesse Cranney, Kevin Schawinski, and Roberta Raileanu. AstroLLaMA: Towards Specialized Foundation Models in Astronomy. In Tirthankar Ghosal, Felix Grezes, Thomas Allen, Kelly Lockhart, Alberto Accomazzi, and Sergi Blanco-Cuaresma (eds.), *Proceedings of the Second Workshop on Information Extraction from Scientific Publications*, pp. 49–55, Bali, Indonesia, November 2023b. Association for Computational Linguistics. doi: 10.18653/v1/2023.wiesp-1.7.

Tung Nguyen, Johannes Brandstetter, Ashish Kapoor, Jayesh K. Gupta, and Aditya Grover. ClimaX: A foundation model for weather and climate. In *Proceedings of the 40th International Conference on Machine Learning*, pp. 25904–25938. PMLR, July 2023c. doi: 10.48550/arXiv.2301.10343.

Ruben Ohana, Michael McCabe, Lucas Thibaut Meyer, Rudy Morel, Fruzsina Julia Agocs, Miguel Beneitez, Marsha Berger, Blakesley Burkhart, Stuart B. Dalziel, Drummond Buschman Fielding, Daniel Fortunato, Jared A. Goldberg, Keiya Hirashima, Yan-Fei Jiang, Rich Kerswell, Suryanarayana Maddu, Jonah M. Miller, Payel Mukhopadhyay, Stefan S. Nixon, Jeff Shen, Romain Watteaux, Bruno Régaldo-Saint Blancard, François Rozet, Liam Holden Parker, Miles Cranmer, and Shirley Ho. The Well: A Large-Scale Collection of Diverse Physics Simulations for Machine Learning. In *The Thirty-eight Conference on Neural Information Processing Systems Datasets and Benchmarks Track*, November 2024. doi: 10.48550/arXiv.2412.00568.

Michael Penwarden, Shandian Zhe, Akil Narayan, and Robert M. Kirby. A metalearning approach for Physics-Informed Neural Networks (PINNs): Application to parameterized PDEs. *Journal of Computational Physics*, 477:111912, March 2023. ISSN 00219991. doi: 10.1016/j.jcp.2023.111912.

Alec Radford, Karthik Narasimhan, Tim Salimans, and Ilya Sutskever. Improving Language Understanding by Generative Pre-Training. 2018.

Alec Radford, Jeffrey Wu, Rewon Child, David Luan, Dario Amodei, and Ilya Sutskever. Language Models are Unsupervised Multitask Learners. 2019.

Colin Raffel, Noam Shazeer, Adam Roberts, Katherine Lee, Sharan Narang, Michael Matena, Yanqi Zhou, Wei Li, and Peter J. Liu. Exploring the Limits of Transfer Learning with a Unified Text-to-Text Transformer. *Journal of Machine Learning Research*, 21(140):1–67, 2020. ISSN 1533-7928.

M. Raissi, P. Perdikaris, and G.E. Karniadakis. Physics-informed neural networks: A deep learning framework for solving forward and inverse problems involving nonlinear partial differential equations. *Journal of Computational Physics*, 378:686–707, February 2019. ISSN 00219991. doi: 10.1016/j.jcp.2018.10.045.

Aditya Ramesh, Mikhail Pavlov, Gabriel Goh, Scott Gray, Chelsea Voss, Alec Radford, Mark Chen, and Ilya Sutskever. Zero-Shot Text-to-Image Generation. In *Proceedings of the 38th International Conference on Machine Learning*, pp. 8821–8831. PMLR, July 2021.

Shashank Subramanian, Peter Harrington, Kurt Keutzer, Wahid Bhimji, Dmitriy Morozov, Michael W Mahoney, and Amir Gholami. Towards foundation models for scientific machine learning: Characterizing scaling and transfer behavior. In A. Oh, T. Naumann, A. Globerson, K. Saenko, M. Hardt, and S. Levine (eds.), *Advances in Neural Information Processing Systems*, volume 36, pp. 71242–71262. Curran Associates, Inc., 2023. doi: 10.48550/arXiv.2306.00258.

Ashish Vaswani, Noam Shazeer, Niki Parmar, Jakob Uszkoreit, Llion Jones, Aidan N Gomez, Lukasz Kaiser, and Illia Polosukhin. Attention is All you Need. In *Advances in Neural Information Processing Systems*, volume 30. Curran Associates, Inc., 2017. doi: 10.48550/arXiv.1706.03762.

Jason Wei, Yi Tay, Rishi Bommasani, Colin Raffel, Barret Zoph, Sebastian Borgeaud, Dani Yogatama, Maarten Bosma, Denny Zhou, Donald Metzler, Ed H. Chi, Tatsunori Hashimoto, Oriol Vinyals, Percy Liang, Jeff Dean, and William Fedus. Emergent Abilities of Large Language Models. *Transactions on Machine Learning Research*, October 2022. ISSN 2835-8856. doi: 10.48550/arXiv.2206.07682.

Runlong Yu, Chonghao Qiu, Robert Ladwig, Paul Hanson, Yiqun Xie, and Xiaowei Jia. Physics-Guided Foundation Model for Scientific Discovery: An Application to Aquatic Science. *Proceedings of the AAAI Conference on Artificial Intelligence*, 39(27):28548–28556, April 2025. ISSN 2374-3468. doi: 10.1609/aaai.v39i27.35078.

6 Appendix

6.1 Limitations

While $\text{GP}_{\text{hy}}\text{T}$ demonstrates promising advances toward true physics foundation models, several key limitations remain:

2D data constraints: Due to data scarcity and computational limitations, the current model is restricted to 2D systems. However, the proposed architecture is directly extensible to 3D systems, and the increased computational demands can be mitigated by employing larger temporal patch sizes.

Long-term stability: Although $\text{GP}_{\text{hy}}\text{T}$ achieves remarkable accuracy in long-term rollout predictions, it falls considerably short of the precision exhibited by numerical solvers. Significantly lower prediction errors are essential for practical engineering applications.

Limited physics coverage: $\text{GP}_{\text{hy}}\text{T}$ is currently trained exclusively on fluid dynamics and heat transfer systems. A comprehensive physics foundation model would require incorporation of diverse physical domains, including mechanics, chemistry, molecular dynamics, and optics.

Fixed domain resolution: The model is trained on 256×128 resolution images. While this resolution is adequate for many simulation scenarios, widespread adoption may necessitate a model capable of handling variable domain sizes and resolutions.

6.2 Results per dataset

Tables 6.2, 6.2, and 6.2 breaks down the performance of the models across the individual test datasets using average MSE, median MSE and averaged variance-weighted RMSE, respectively. Overall, $\text{GP}_{\text{hy}}\text{T}$ demonstrates robust performance, achieving low MSEs across a wide range of physics. Systems such as obstacle flow and shear flow show exceptionally low errors, indicating the model captures their dynamics with high fidelity.

More complex systems involving heat transfer, such as Rayleigh-Bénard, or the Euler dataset, which features shockwaves and sharp discontinuities, present a greater challenge, resulting in a higher errors. This is expected, as such phenomena are notoriously difficult to resolve accurately.

Table 3: Averaged MSE across all test samples for single timestep prediction. Lower is better.

Dataset	$\textbf{GP}_{\textbf{hy}}\textbf{T-S}$ 9.2M	**FNO-M** 118M	**Unet-M** 124M	$\textbf{GP}_{\textbf{hy}}\textbf{T-M}$ 112M	$\textbf{GP}_{\textbf{hy}}\textbf{T-L}$ 385M	$\textbf{GP}_{\textbf{hy}}\textbf{T-XL}$ 796M
Obstacle flow	9.06e-4	5.94e-3	7.35e-4	3.18e-4	2.09e-4	1.80e-4
Shear flow	8.57e-4	1.08e-2	4.20e-4	2.11e-4	1.22e-4	1.02e-4
Thermal flow	2.68e-3	2.25e-2	1.79e-3	1.24e-3	9.16e-4	8.32e-4
Twophase flow	1.02e-2	2.22e-2	3.89e-3	5.94e-3	5.00e-3	4.62e-3
Rayleigh–Bénard	1.59e-2	5.29e-2	9.95e-3	8.23e-3	6.54e-3	6.14e-3
Euler	4.10e-2	1.15e-1	1.70e-2	1.50e-2	1.03e-2	8.92e-3
Average	1.19e-2	3.83e-2	5.63e-3	5.16e-3	3.85e-3	**3.46e-3**

Table 4: Median MSE across all test samples for single timestep prediction. Lower is better.

Dataset	**GP$_{\text{hy}}$T-S** 9.2M	**FNO-M** 118M	**Unet-M** 124M	**GP$_{\text{hy}}$T-M** 112M	**GP$_{\text{hy}}$T-L** 385M	**GP$_{\text{hy}}$T-XL** 796M
Obstacle flow	1.96e-5	1.97e-4	1.64e-4	5.74e-6	2.91e-6	2.22e-6
Shear flow	5.94e-5	6.10e-4	8.54e-5	1.47e-5	8.52e-6	6.94e-6
Thermal flow	3.86e-4	4.25e-3	4.64e-4	1.40e-4	9.70e-5	8.23e-5
Twophase flow	8.78e-5	8.70e-4	5.37e-4	3.46e-5	2.20e-5	1.85e-5
Rayleigh–Bénard	7.38e-4	4.67e-3	7.72e-4	2.60e-4	1.73e-4	1.46e-4
Euler	2.06e-2	6.61e-2	6.90e-3	6.67e-3	4.24e-3	3.51e-3
Average	2.37e-4	2.56e-3	5.00e-4	8.74e-5	5.95e-5	**5.04e-5**

Table 5: Averaged variance-weighted RMSE across all test samples for single timestep prediction. Lower is better.

Dataset	**GP$_{\text{hy}}$T-S** 9.2M	**FNO-M** 118M	**Unet-M** 124M	**GP$_{\text{hy}}$T-M** 112M	**GP$_{\text{hy}}$T-L** 385M	**GP$_{\text{hy}}$T-XL** 796M
Obstacle flow	3.93e-2	9.81e-2	9.45e-1	2.36e-2	1.77e-2	1.55e-2
Shear flow	2.57e-1	6.37e-1	4.22e-1	1.68e-1	1.28e-1	1.05e-1
Thermal flow	5.16e-2	1.17e-1	7.55e-2	3.52e-2	3.01e-2	2.78e-2
Twophase flow	6.73e-2	1.71e-1	1.12e-1	4.57e-2	3.49e-2	3.12e-2
Rayleigh–Bénard	1.58e-1	3.55e-1	1.69e-1	9.68e-2	7.73e-2	7.08e-2
Euler	2.44e-1	4.23e-1	1.51e-1	1.43e-1	1.15e-1	1.05e-1
Average	1.36e-1	3.00e-1	1.70e-1	8.54e-2	6.71e-2	**5.91e-2**

6.3 PROMPT SIZE

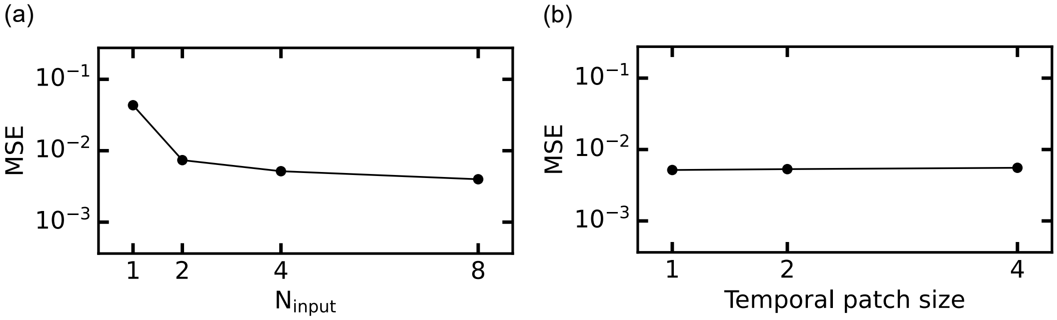

Figure 6: (a) Average MSE over the full test set for different number of input time steps (N$_{\text{input}}$) with a temporal patch size of 1. (b) Average MSE over the full test set for 4 input time steps and increasing temporal patch size.

The capacity for in-context learning is central to GP$_{\text{hy}}$T's generality, and this capacity is directly governed by the input prompt. An effective prompt must provide sufficient spatiotemporal information for the model to infer the system's underlying dynamics, yet remain computationally tractable. This presents a challenge, as the transformer's self-attention mechanism scales quadratically with the input sequence length, making long prompts computationally expensive. Furthermore, since the prompt itself must be generated by a numerical solver at inference time, minimizing its length is critical for practical applications.

We investigated this trade-off by varying the number of input timesteps (N_{input}) and the temporal patch size. Figure 6a shows the model's performance as a function of N_{input}. A single input timestep ($N_{\text{input}} = 1$), which provides no dynamic context, yields the highest error. The most significant performance gain occurs when increasing the prompt from one to two timesteps, confirming that even minimal temporal context is crucial for the model to infer the system's evolution. As the prompt length increases further, performance continues to improve in a log-linear fashion, albeit with diminishing returns.

To mitigate the computational burden of longer prompts, we can increase the temporal patch size, which embeds multiple consecutive timesteps into a single token, thereby reducing the effective sequence length. As shown in Figure 6b, increasing the temporal patch size from 1 to 4 for a fixed prompt of four total timesteps leads to only a minor decrease in accuracy. This demonstrates a valuable trade-off: by compressing temporal information into patches, we can significantly reduce computational and memory requirements with a negligible impact on performance. These hyperparameters provide crucial levers for balancing predictive accuracy against computational cost, allowing for adaptation to different resource constraints.

6.4 Integrator schemes

We conducted an ablation study to determine the effect of the numerical integration scheme on model performance. Two main strategies were compared: (1) a baseline approach where the Transformer directly predicts the next system state, X_{t+1}, and (2) the proposed framework where the model acts as a neural differentiator, predicting the time derivative $\frac{\partial X}{\partial t}$, which is then advanced in time by a numerical integrator. For the differentiator-integrator framework, we evaluated three explicit methods of increasing order: Forward Euler (first-order), Heun's method (second-order), and the fourth-order Runge-Kutta (RK4) method. Each model (variant M) was trained for 600,000 updates, and the results are shown in Figure 7.

The study reveals two key findings. First, decoupling the prediction into differentiation and integration provides a substantial performance benefit. All models using the neural differentiator framework significantly outperformed the direct prediction baseline. Second, among the tested numerical integrators, increasing the order and computational complexity from first-order Euler to fourth-order RK4 did not yield a corresponding improvement in prediction accuracy. Since the simple Forward Euler method achieved comparable accuracy to the more complex schemes with the lowest computational cost, it was selected for all other experiments in this work.

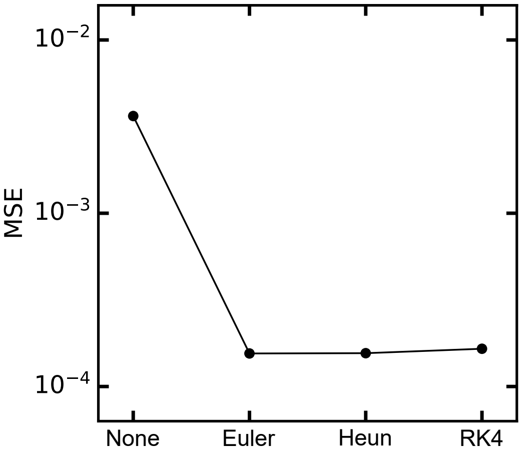

Figure 7: Median MSE on the test set for different integration strategies. The baseline "None" model directly predicts the next time step. The Euler, Heun, and RK4 models predict the time derivative $\frac{\partial X}{\partial t}$, which is then used by the corresponding numerical integrator. The differentiator-integrator approach is clearly superior, with minimal difference between the specific integrator schemes.

6.5 Model & training hyperparameters

6.5.1 General Physics Transformer

For the models S, M, and L, we train on 4 Nvidia H100 or A100-80GB in parallel. For the XL model, we train on 4 Nvidia H200. We always use a combined batch size of 256. Due to the size of each

Table 6: GP$_{\text{hy}}$T parameters with number of transformer layers, size of embedding (patch) dimension, size of MLP dimension, and number of heads in the multi-head attention. Tflops represent the number of teraflops per update (forwards & backwards).

Model	#params [M]	Num layers	Embedding dim	MLP dim	Num heads	Tflops
S	9.2	12	192	768	3	123.52
M	112	12	768	3072	12	698.56
L	385	24	1024	4096	16	1,567.24
XL	796	32	1280	5120	16	2,791.84

Table 7: Training and model hyperparameter

Pos. encodings	absolute
Activation function	GELU
Norm	Layer norm
Optimizer	AdamW ($\beta_1 = 0.9, \beta_2 = 0.999$)
Learning rate	lin. warmup (5K steps), then cosine decay to 1e-6
Batch size	256
Precision	bfloat16
Gradient norm (L^2)	1
Dropout	no
Stochastic depth (Huang et al., 2016)	no

sample (4-dimensional), at minimum 16 dataloader workers are used to fetch the samples. Training and evaluation was done with Pytorch 2.7. We used linear warmup of the learning rate over 5000 steps to 1e-4. After that, a cosine decay schedule with a final learning rate of 1e-6 was used. To stabilize the training, we employ gradient normalization using L^2 norm equal to 1. A complete list of model parameter is given in Table 6 and additional hyperparameters are given in Table 7. Teraflops are calculated for a full (multi-gpu) batch with the compiled model and bfloat16 using the torchtnt library.

6.5.2 Reference models

We use the 3D-FNO proposed in Li et al. (2020) with code from the official FNO repository (Kossaifi et al., 2025). The FNO was trained on 4 H100 in parallel. Due to the significantly higher computational cost, batch size was reduced to 128 for the FNO. The Unet model is a standard architecture: Each downsample block doubles the number of channels and halfs the spatial resolution. The upsample block revert this process with skip connections between the corresponding down and upsample blocks. We employ 2D convolutions and thus the time steps are flattened into the channel dimension. For both models, learing rate and gradient clipping were equal to the GP$_{\text{hy}}$T training.

Table 8: FNO model parameters

Model	Parameters [M]	Num layers	Embedding dim	Num modes
FNO-M	118	4	128	15

6.6 Dataset Details

All datasets used to train the models comprise of a timeseries (T) of 2D ($H \times W$) snapshots of a physical domain goverend by common PDE equations such as Navier-Stokes, heat equation or surface tension. Thus, each dataset sample has the form

$$x \in \mathbb{R}^{T \times H \times W \times X} \tag{2}$$

Table 9: UNet model parameters

Model	Parameters [M]	Num down/up blocks	Hidden dim at start/end
Unet-M	124	4	64

were X are the physical fields, in our case pressure, density, temperature, velocity-x, and velocity-y. Fields not present in the simulation data are provided as zeroed. For training, spatial dimensions of 256 x 128 pixels were used. Datasets with originally larger dimensions were interpolated using bicubic interpolation. Additionally, the Figures 8 and 9 illustrate the general conditions and boundaries of the-well and our simulations, respectively. Each trajectory can be sampled with different Δt, thus for a given number of snapshots N_{total}, a number of input (N_{in}) and output snapshots (N_{out}) and a given Δt, $N_{total} - \Delta t(N_{in} + N_{out} - 1)$ unique samples can be generated. Additionally, we employ random axis flips to further increase the diversity of the data. All datasets are split into train/val/test with ratios of 0.8/0.1/0.1.

6.6.1 Incompressible shear flow

The shearflow dataset (Ohana et al., 2024) considers a 2D-periodic incompressible shear flow, visualized in Figure 8a). The velocity $\mathbf{u} = (u_x, u_z)$ (horizontal and vertical) and pressure p are governed by the Navier-Stokes equation

$$\frac{\partial \mathbf{u}}{\partial t} - \nu \Delta \mathbf{u} + \nabla p = -(\mathbf{u} \cdot \nabla)\mathbf{u} \tag{3}$$

with the additional constraint $\int p \, dV = 0$ for the pressure gauge. Here, $\Delta = \nabla \cdot \nabla$ is the spatial Laplacian, and ν is the kinematic viscosity. The shear is initialized by setting the velocity $\mathbf{u}$ in different fluid layers to move in opposite vertical directions. Density and temperature are not considered and thus zeroed in the models input.

6.6.2 Multiquadrant Euler

The Euler equations describe inviscid compressible flow governed by

$$\frac{\partial}{\partial t} \iint_{\Omega} U \, dA + \oint_{\partial\Omega} (F\hat{i} + G\hat{j}) \cdot \hat{n} \, dS = 0 \tag{4}$$

$$\tag{5}$$

where

$$U = \begin{pmatrix} \rho \\ \rho u \\ \rho v \\ \rho E \end{pmatrix} \quad \text{and} \quad F = \begin{pmatrix} \rho u \\ \rho u^2 + p \\ \rho uv \\ u(\rho E + p) \end{pmatrix} \quad G = \begin{pmatrix} \rho v \\ \rho uv \\ \rho v^2 + p \\ v(\rho E + p) \end{pmatrix} \tag{6}$$

Here, t is time, Ω is the control volume with boundary $\partial\Omega$, A is the area, and S is the boundary length. U is the vector of conserved variables, F and G are the flux vectors in the x and y directions respectively, $\hat{i}$ and $\hat{j}$ are the unit vectors in the x and y directions, and $\hat{n}$ is the outward normal vector to the boundary. The conserved variables are density ρ, momentum in the x-direction ρu, momentum in the y-direction ρv, and total energy per unit volume ρE, where u and v are the velocity components in the x and y directions, and E is the specific total energy. The pressure is denoted by p.

In this dataset (Ohana et al., 2024), the initial pressure field is divided into quadrants with different pressure values, leading to shock waves and other discontinuities. All boundaries are considered as periodic, visualized in Figure 8b). In the original dat, momentum (x,y) was given and thus converted to velocity. Since the system is isothermal, the temperature field is zeroed.

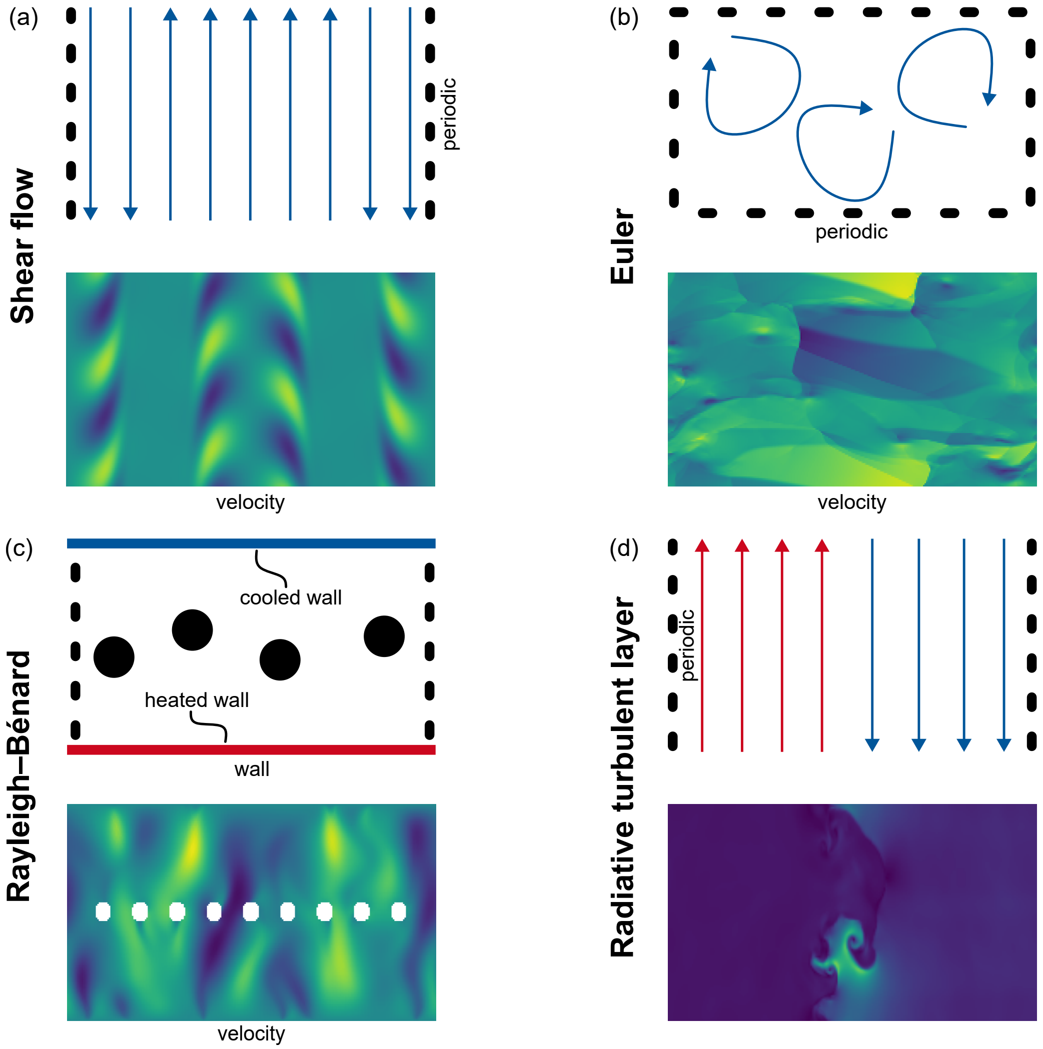

Figure 8: Illustration of physical domain and boundary conditions of the-well datasets. (a) Shearflow with periodic boundary conditions. (b) Simulation of Euler equations initialized with pressure quadrants and periodic boundary conditions. (c) Rayleigh–Bénard convection with heated bottom and cooled top wall, as well as randomly placed obstacles, and periodic boundaries. (d) Turbulent radiative layer with hot and cold gas moving in opposite directions.

6.6.3 Rayleigh–Bénard

Rayleigh–Bénard (Figure 8d) convection occurs between two plates with different temperatures. It is governed by heat transport and fluid flow. Depending on the initial conditions, even tiny variations in temperature or pressure can lead to vastly different fluid behavior. This dataset combines data from the-well (Ohana et al., 2024), which contains no obstacles, and our own data with obstacles.

The governing equations are:

$$\frac{\partial b}{\partial t} - \kappa \Delta b = -\mathbf{u} \cdot \nabla b \tag{7}$$

$$\frac{\partial \mathbf{u}}{\partial t} - \nu \Delta \mathbf{u} + \nabla p - b\mathbf{e}_z = -\mathbf{u} \cdot \nabla \mathbf{u} \tag{8}$$

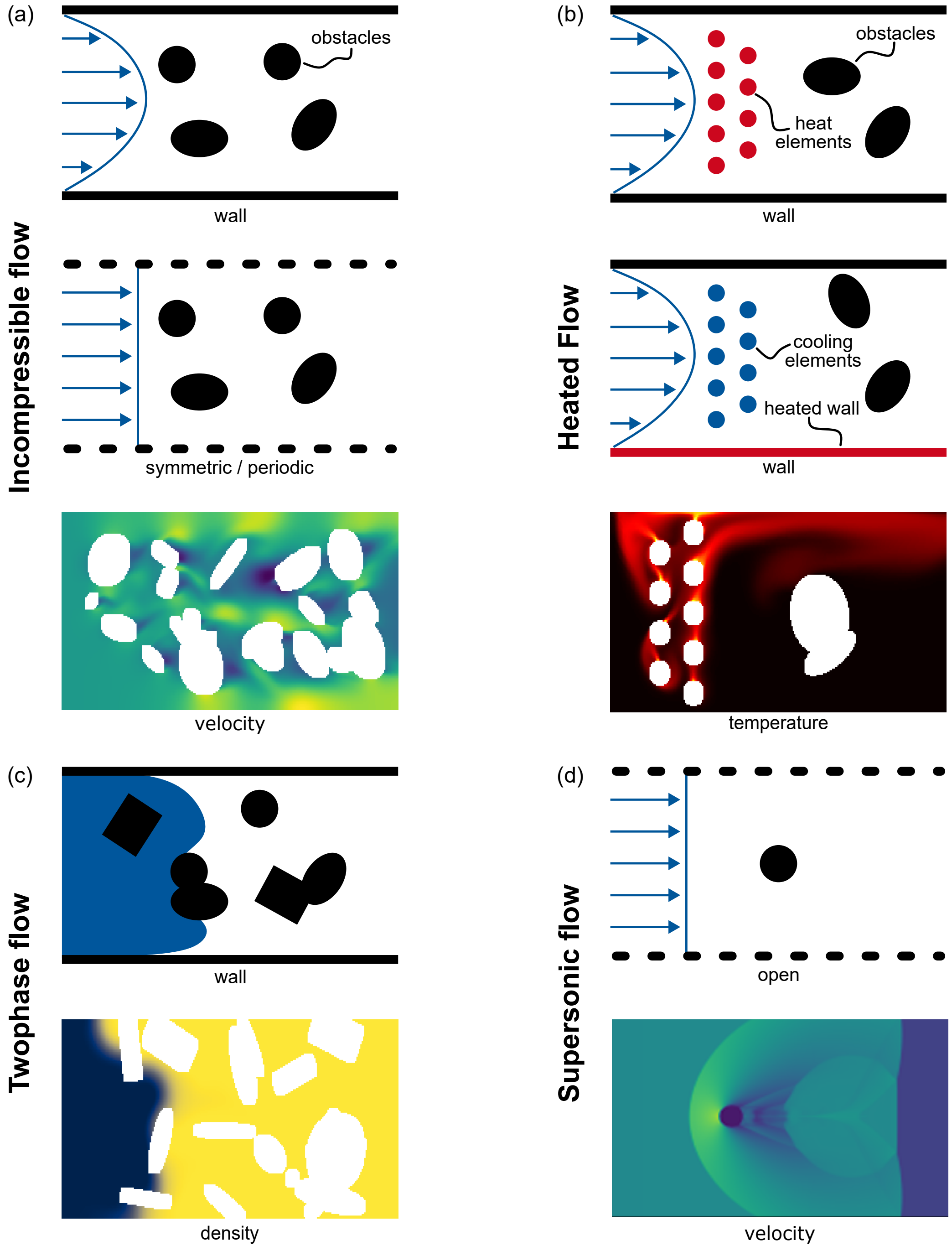

Figure 9: Illustration of physical domain and boundary conditions of our datasets. (a) Incompressible flow around a series of randomly placed obstacles, boundary conditions vary between walls, symmetric, and periodic. (b) Heated flow inside a pipe (walls) with heated elements or walls and isolated obstacles. (c) Twophase flow in random porous media. (d) Supersonic flow with a shock wave hitting a cylinder.

with $\Delta = \nabla \cdot \nabla$ and the constraint $\int p \, dV = 0$. The parameters κ and ν are given by:

$$\kappa = \text{Ra} \times \text{Pr}^{-1/2} \tag{9}$$

$$\nu = \text{Ra}^{1/2} \times \text{Pr}^{-1/2} \tag{10}$$

Here, b represents buoyancy, κ is the thermal diffusivity, and ν is the kinematic viscosity. The velocity vector of the fluid is denoted by $\mathbf{u}$, and p is the pressure. The upward vertical unit vector is given by $\mathbf{e}_z$. The dimensionless parameters governing the system are the Rayleigh number, denoted by Ra, and the Prandtl number, denoted by Pr.

6.6.4 Turbulent Radiative Layer

The turbulent radiative layer dataset considers a 2D system where hot dilute gas moves relative to cold dense gas, leading to turbulent mixing and radiative cooling processes commonly found in astrophysical environments such as the interstellar and circumgalactic medium, visualized in Figure 8d). This configuration is unstable to the Kelvin-Helmholtz instability, which is seeded with small-scale noise that varies between simulations. The system is governed by the compressible Euler equations with radiative cooling:

$$\frac{\partial \rho}{\partial t} + \nabla \cdot (\rho \mathbf{v}) = 0 \tag{11}$$

$$\frac{\partial (\rho \mathbf{v})}{\partial t} + \nabla \cdot (\rho \mathbf{v}\mathbf{v} + P\mathbf{I}) = 0 \tag{12}$$

$$\frac{\partial E}{\partial t} + \nabla \cdot ((E + P)\mathbf{v}) = -\frac{E}{t_{\text{cool}}} \tag{13}$$

with the equation of state

$$E = \frac{P}{\gamma - 1}, \quad \gamma = \frac{5}{3} \tag{14}$$

Here, ρ is the density, $v = (u, v)$ is the 2D velocity vector, P is the pressure, E is the total energy per unit volume, I is the identity tensor, and t_{cool} is the cooling time parameter that controls the rate of radiative energy loss.

Initially, cold dense gas is positioned at the bottom while hot dilute gas occupies the top region. Both phases are in thermal equilibrium until mixing occurs, whereupon intermediate temperature gas forms and experiences net cooling, leading to mass transfer from the hot to cold phase. The boundary conditions are periodic in the x-direction with zero-gradient conditions in the y-direction.

6.6.5 Incompressible Flow with Obstacles

The dataset include various flow simulations described by the incompressible Navier-Stokes equation and modeled in Comsol 6.3.

$$\begin{aligned} \nabla \cdot \vec{u} &= 0 \\ \frac{\partial \vec{u}}{\partial t} + (\vec{u} \cdot \nabla)\vec{u} &= -\frac{1}{\rho}\nabla p + \nu \nabla^2 \vec{u} + \vec{f} \end{aligned}$$

Solid obstacles described by no-slip wall conditions obstruct and alter the flow. The boundary conditions at y=0 and y=-1 vary from simulation to simulation and can either be wall, symmetric or periodic. The inlet at x=0 is defined by an inlet velocity. For the wall case, the inlet velocity is parabular-shaped. The system is incompressible and isothermal, yielding zeroed density and temperature fields.

6.6.6 Heated Flow

Heated flow (Figure 9b) is an extension of the incompressible flow around obstacles. Here, a compressible gas is heated/cooled while flowing through a channel with obstacles. This creates interesting interactions of density-driven convection and the forced convection. Two versions of the systems are used, one with heating rods (top) and one with cooling rods and a heated wall (middle).

Governing equations are the compressible Navier-Stokes equations for conservation of mass, momentum, and energy:

$$\frac{\partial \rho}{\partial t} + \nabla \cdot (\rho \mathbf{u}) = 0 \tag{15}$$

$$\frac{\partial (\rho \mathbf{u})}{\partial t} + \nabla \cdot (\rho \mathbf{u} \otimes \mathbf{u} + p\mathbf{I}) = \nabla \cdot \tau + \rho \mathbf{g} \tag{16}$$

$$\frac{\partial E}{\partial t} + \nabla \cdot ((E + p)\mathbf{u}) = \nabla \cdot (\tau \cdot \mathbf{u} - \mathbf{q}) + \rho \mathbf{g} \cdot \mathbf{u} \tag{17}$$

and the heat conduction equation, which is part of the energy equation above, is described by Fourier's law:

$$\mathbf{q} = -k\nabla T$$

where ρ is the fluid density, $\mathbf{u}$ is the flow velocity vector, p is the pressure, $\mathbf{I}$ is the identity tensor, τ is the deviatoric stress tensor, $\mathbf{g}$ is the gravitational acceleration, E is the total energy per unit volume, $\mathbf{q}$ is the heat flux vector, k is the thermal conductivity, and T is the temperature.

6.6.7 TWOPHASE FLOW

Twophase flow in porous media (Figure 9c) is an important problem in energy systems, hydrology and the petro-industry. In this dataset, water replaces air inside a randomly generated pore structure. For contact angles above 90 degrees (hydrophobic), a positive pressure is applied. For hydrophilic contact angles, a negative pressure is applied. The fluid motion is governed by capillary pressure, surface tension and contact angles. This dataset was generated with COMSOL 6.3 using the phase-field method.

The phase field method describes the interface between immiscible fluids using a continuous dimensionless phase field parameter ϕ. The system's free energy is given by the functional

$$F(\phi) = \int_{\Omega} \left(f_{mix}(\phi) + \frac{1}{2}\epsilon^2 |\nabla \phi|^2 \right) dV \tag{18}$$

where ϵ is a measure of the interface thickness, f_{mix} is the mixing free energy density, and the second term accounts for the energy associated with interface gradients.

The evolution of the phase field parameter, including advection by the velocity field $\mathbf{u}$, is governed by the following equation, which aims to minimize the total free energy density f_{tot} (J/m^3) with a relaxation time controlled by the mobility γ $(m^3 \cdot s/kg)$

$$\begin{aligned} \frac{\partial \phi}{\partial t} + \mathbf{u} \cdot \nabla \phi &= \nabla \cdot \left(\gamma \nabla \frac{\delta F}{\delta \phi} \right) \\ &= \nabla \cdot \left(\gamma \nabla \left(\frac{\partial f_{tot}}{\partial \phi} - \epsilon^2 \nabla^2 \phi \right) \right) \end{aligned} \tag{19}$$

Here, f_{tot} is the total free energy density, which includes the mixing energy and potentially other contributions like elastic energy.

For an isothermal mixture of two immiscible fluids, the mixing energy density f_{mix} typically assumes the Ginzburg-Landau form:

$$f_{mix}(\phi) = \lambda \left(1 - \phi^2\right)^2 \tag{20}$$

Here, ϕ is the dimensionless phase field variable, defined such that the volume fractions of the two fluid components are $(1 + \phi)/2$ and $(1 - \phi)/2$. The quantity λ (N) is the mixing energy density, and

ϵ (m) is a capillary width related to the interface thickness. These two parameters are connected to the surface tension coefficient σ (N/m) through the equation

$$\sigma = \frac{2\sqrt{2}}{3}\frac{\sqrt{\lambda}}{\epsilon} \tag{21}$$

When considering only mixing energy and gradient energy, the evolution equation (19) simplifies to the Cahn-Hilliard equation:

$$\frac{\partial \phi}{\partial t} + \mathbf{u} \cdot \nabla \phi = \nabla \cdot (\gamma \nabla G) \tag{22}$$

where G (Pa) is the chemical potential, and γ ($m^3 \cdot s/kg$) is the mobility. The mobility controls the timescale of Cahn-Hilliard diffusion and must be chosen appropriately to maintain a constant interfacial thickness without excessively damping convective terms.

The chemical potential G is given by the derivative of the free energy density with respect to the phase field

$$G = \frac{\partial f_{tot}}{\partial \phi} - \epsilon^2 \nabla^2 \phi \tag{23}$$

The Cahn-Hilliard equation drives ϕ towards values of 1 or -1 in the bulk phases, with a rapid transition occurring within the thin fluid-fluid interface region. The Phase Field interface in COMSOL Multiphysics typically solves equation (22) by splitting it into two coupled second-order PDEs

$$\frac{\partial \phi}{\partial t} + \mathbf{u} \cdot \nabla \phi = \nabla \cdot (\gamma \nabla G) \tag{24}$$

$$G = \frac{\partial f_{mix}}{\partial \phi} - \epsilon^2 \nabla^2 \phi \tag{25}$$

6.6.8 Supersonic flow

Supersonic flow is modeled as compressible inviscid flow. The shock front moves with Mach numbers between 1.1 to 5.0. Governing equations are

$$\frac{\partial}{\partial t}\iint_{\Omega} U\, dA + \oint_{\partial\Omega} (F\hat{i} + G\hat{j}) \cdot \hat{n}\, dS = 0 \tag{26}$$

$$\tag{27}$$

where

$$U = \begin{pmatrix} \rho \\ \rho u \\ \rho v \\ \rho E \end{pmatrix} \quad \text{and} \quad F = \begin{pmatrix} \rho u \\ \rho u^2 + p \\ \rho uv \\ u(\rho E + p) \end{pmatrix} \quad G = \begin{pmatrix} \rho v \\ \rho uv \\ \rho v^2 + p \\ v(\rho E + p) \end{pmatrix} \tag{28}$$

Except for the inlet, Neumann boundary conditions are used (sides and outlet). Initial conditions are set to atmospheric conditions (P = 101325 Pa, T = 298 K, ρ = 1.23 kg/m3). The system is isothermal.

6.7 Detailed Nextstep Predictions

The following results can be best viewed on a high-definition digital monitor.

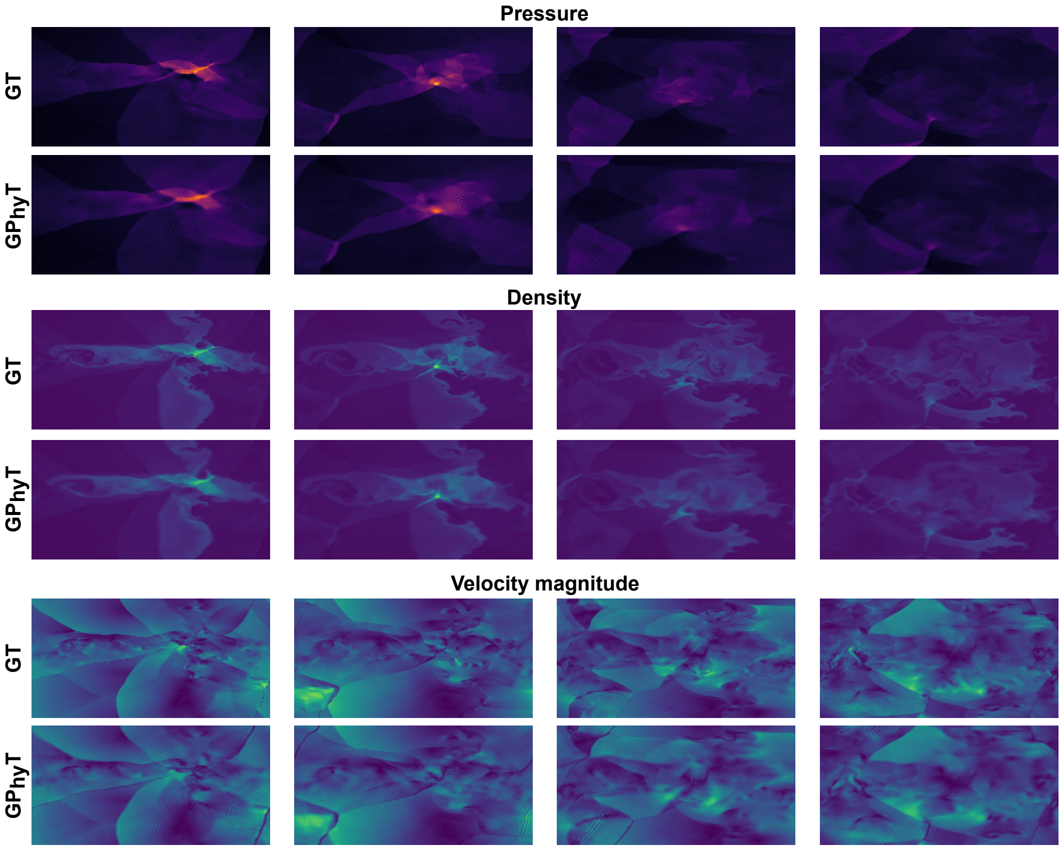

Figure 10: Next step predictions and ground truth (GT) for the Euler dataset for the fields density, pressure, and velocity magnitude (x and y combined) with a Δt of 4. Since Euler equations are isothermal, the temperature is not shown. Predictions are done by GP$_{\text{hy}}$T-M.

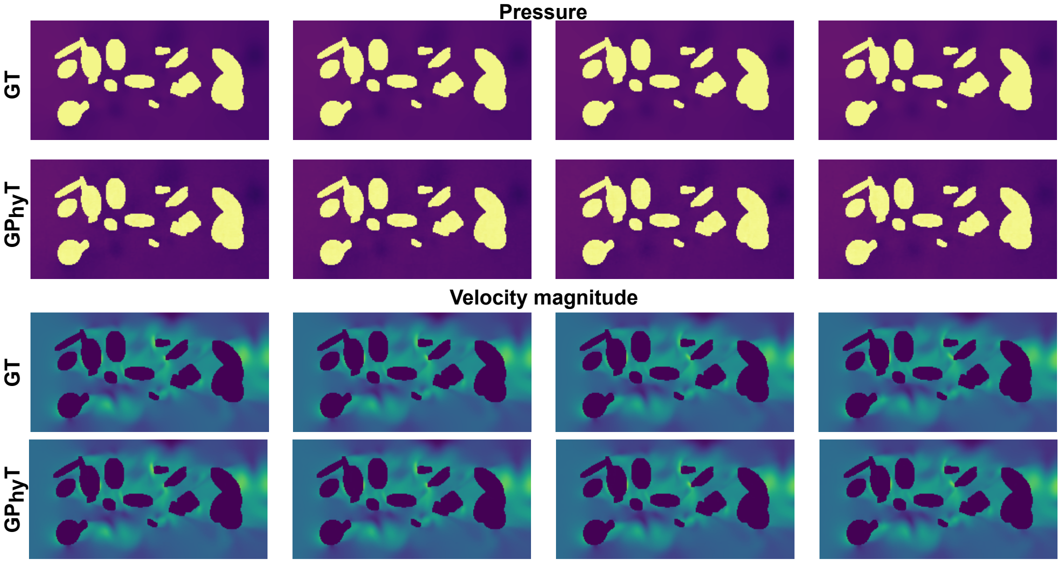

Figure 11: Next step predictions and ground truth (GT) for the incompressible flow dataset for the fields pressure, vel-x, and vel-y with a Δt of 8. Since incompressible flow is isothermal and incompressible, temperature and density fields are not shown. Predictions are done by GP_{hy}T-M.

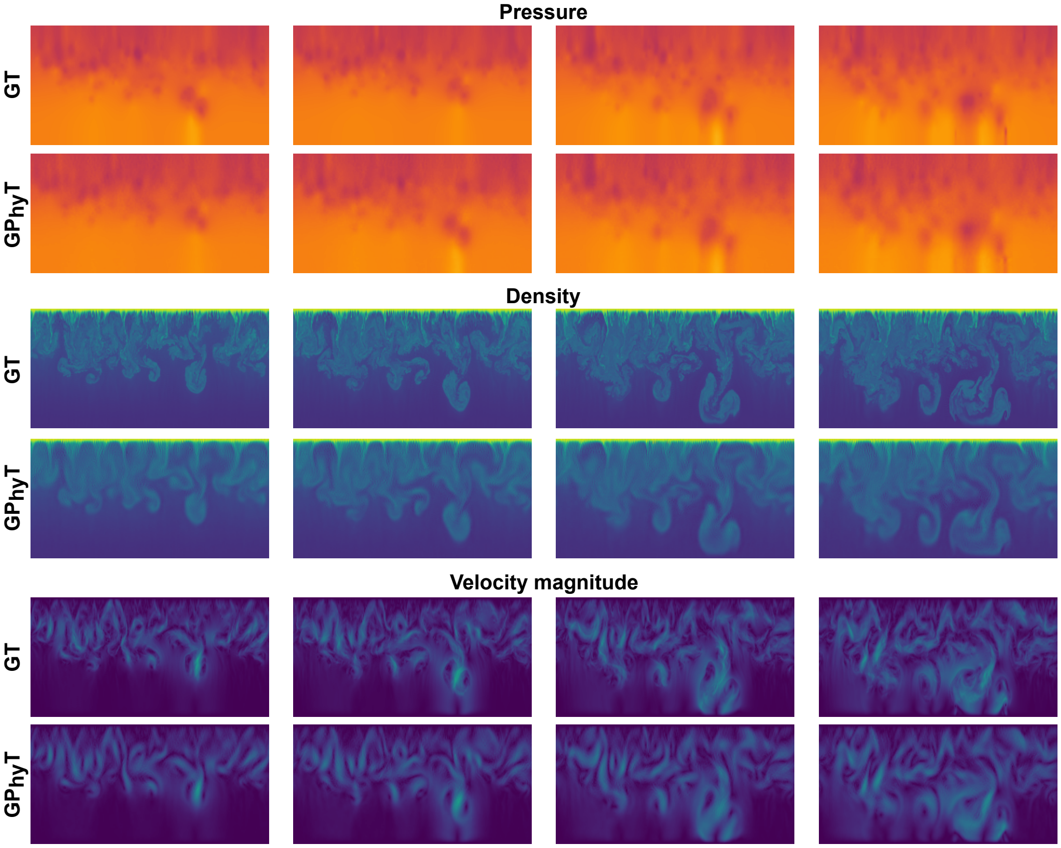

Figure 12: Next step predictions and ground truth (GT) for the Rayleigh–Bénard from the-well dataset for the fields density, pressure, vel-x, and vel-y with a Δt of 8. Predictions are done by GP_{hy}T-M.

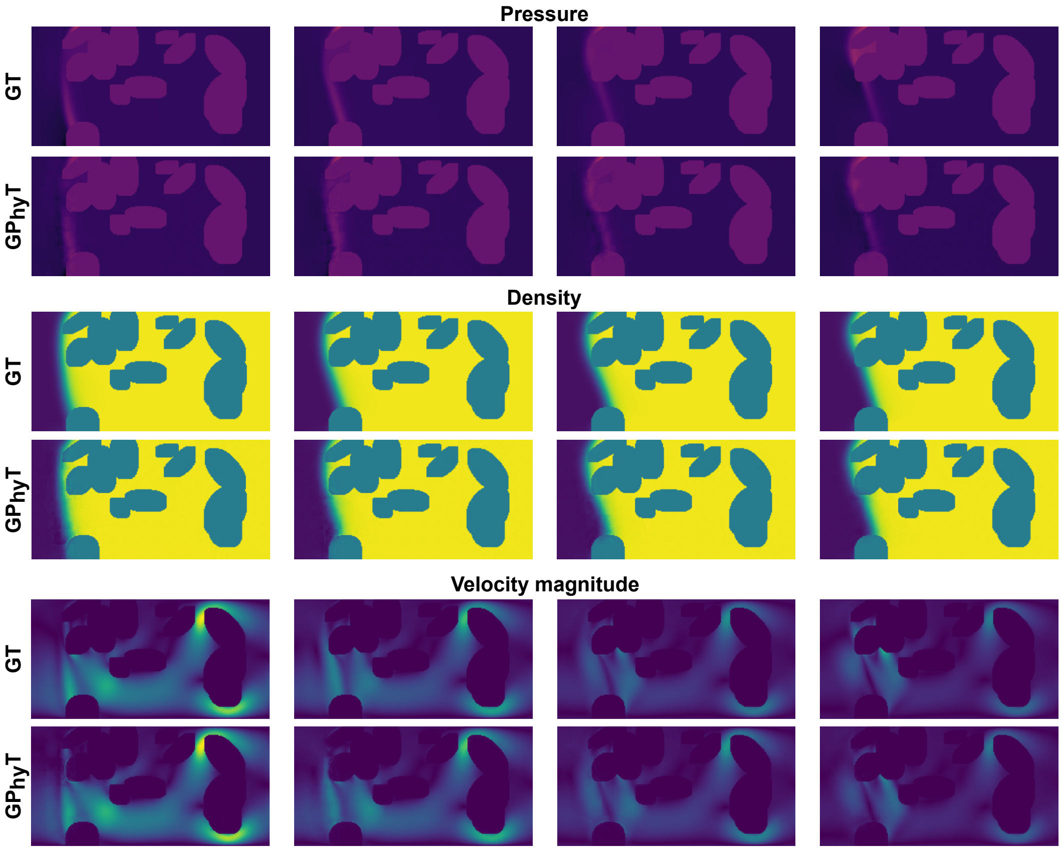

Figure 13: Next step predictions and ground truth (GT) for the twophase flow dataset for the fields density, pressure, and velocity magnitude (x and y combined), with a Δt of 8. Since the twophase flow is considered isothermal, the temperature is not shown. Predictions are done by GP_{hy}T-M.

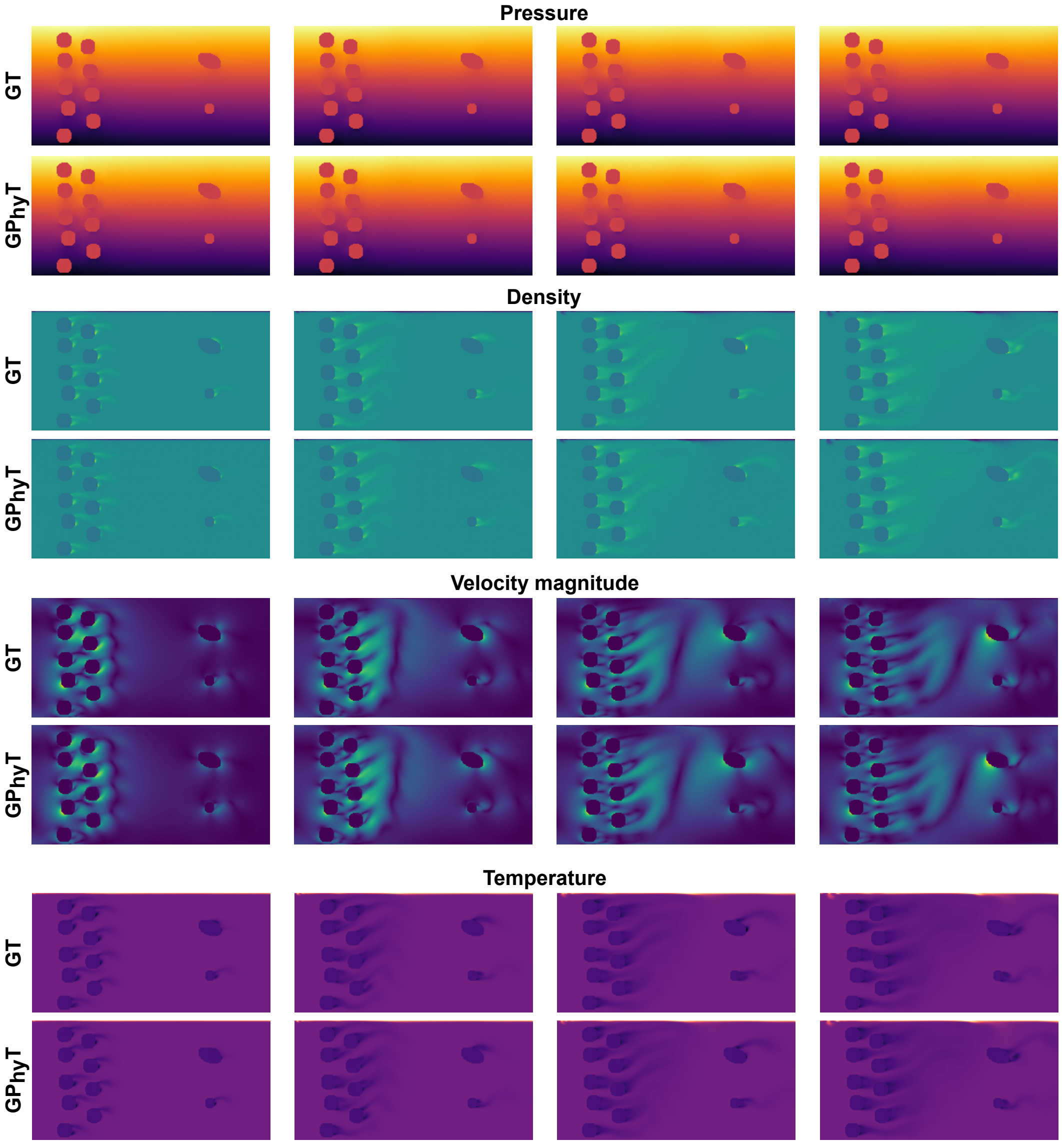

Figure 14: Next step predictions and ground truth (GT) for the heated flow dataset for the fields density, pressure, temperature and velocity magnitude (x and y combined), with a Δt of 8. Predictions are done by GP_{hy}T-M.

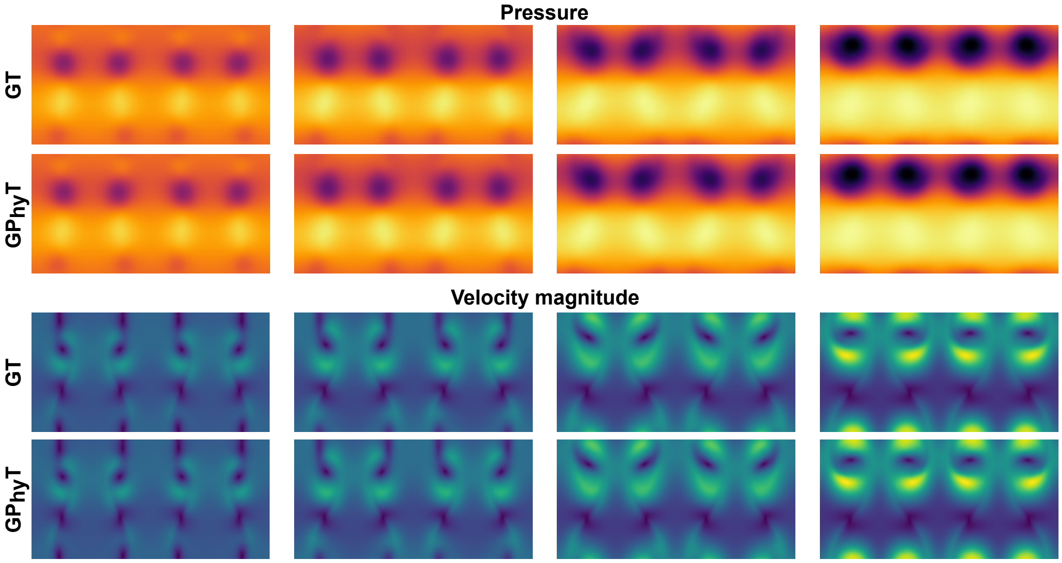

Figure 15: Next step predictions and ground truth (GT) for the shearflow dataset for the fields pressure, and velocity magnitude (x and y combined), with a Δt of 8. Predictions are done by GP$_{\text{hy}}$T-M.

6.8 Detailed Predictions for Unknown Physics

The following results can be best viewed on a high-definition digital monitor.

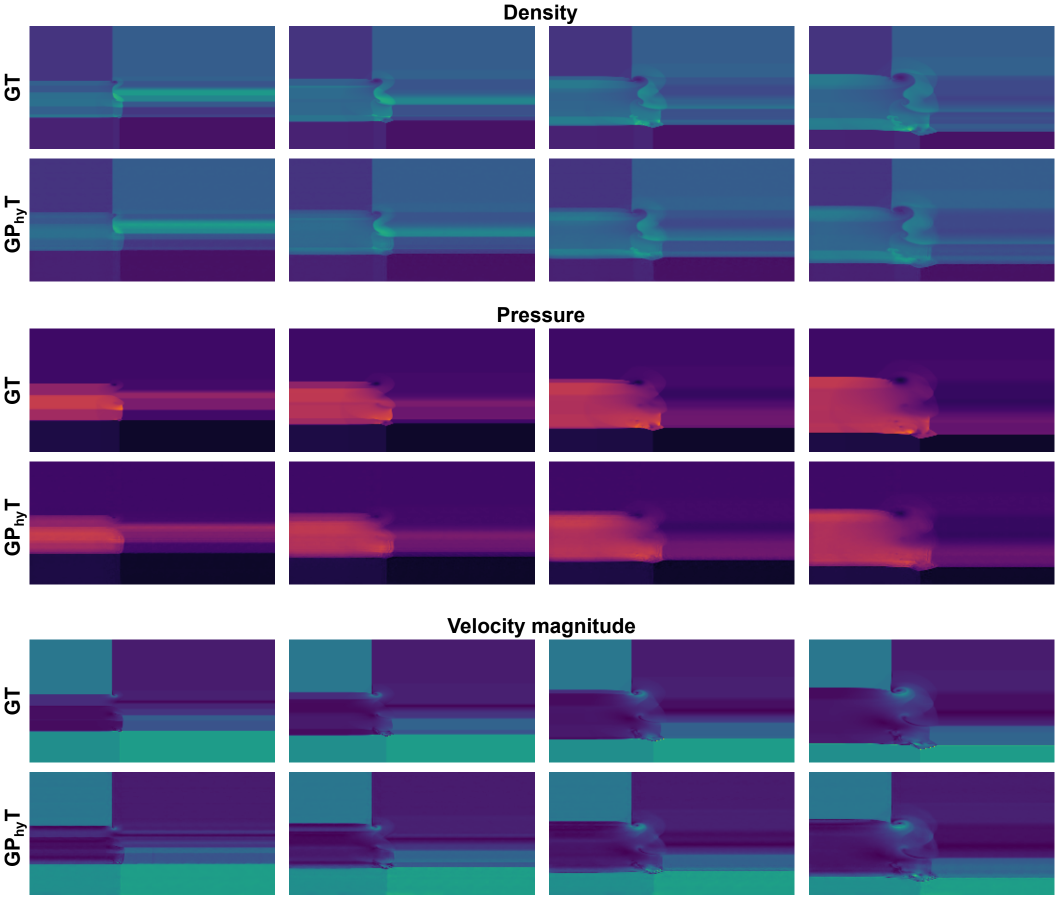

Figure 16: Next step predictions and ground truth (GT) for the novel Euler system with open boundary conditions for the fields density, pressure, and velocity magnitude (x and y combined), with a Δt of 1. Predictions are done by GP$_{\text{hy}}$T-XL.

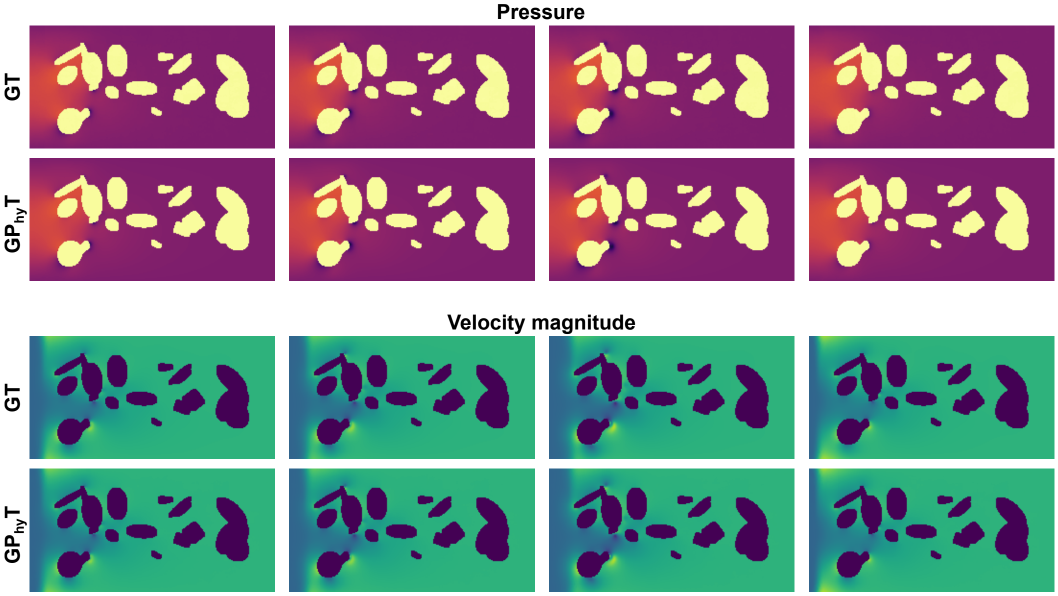

Figure 17: Next step predictions and ground truth (GT) for the novel flow around obstacles with open boundary conditions for the fields pressure and velocity magnitude (x and y combined), with a Δt of 1. Predictions are done by GP$_{\text{hy}}$T-XL.

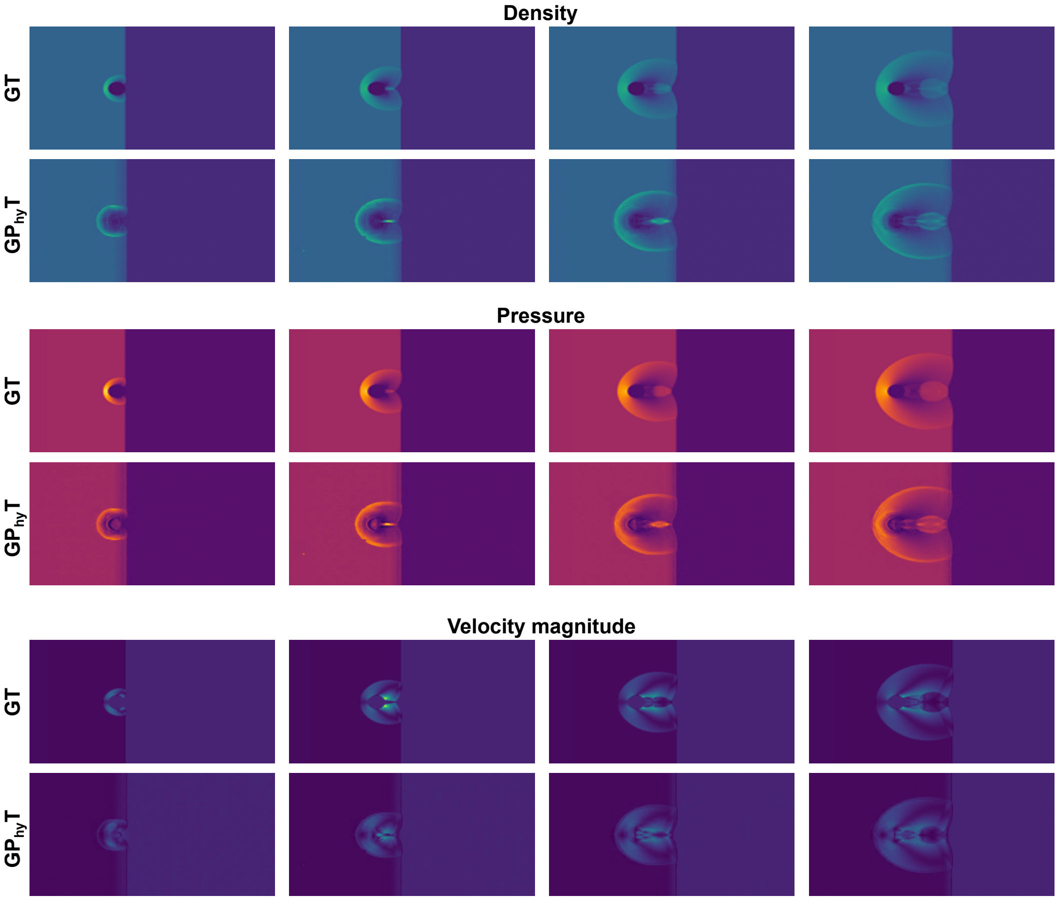

Figure 18: Next step predictions and ground truth (GT) for the novel supersonic flow system for the fields density, pressure, and velocity magnitude (x and y combined), with a Δt of 1. Predictions are done by GP$_{\text{hy}}$T-XL.

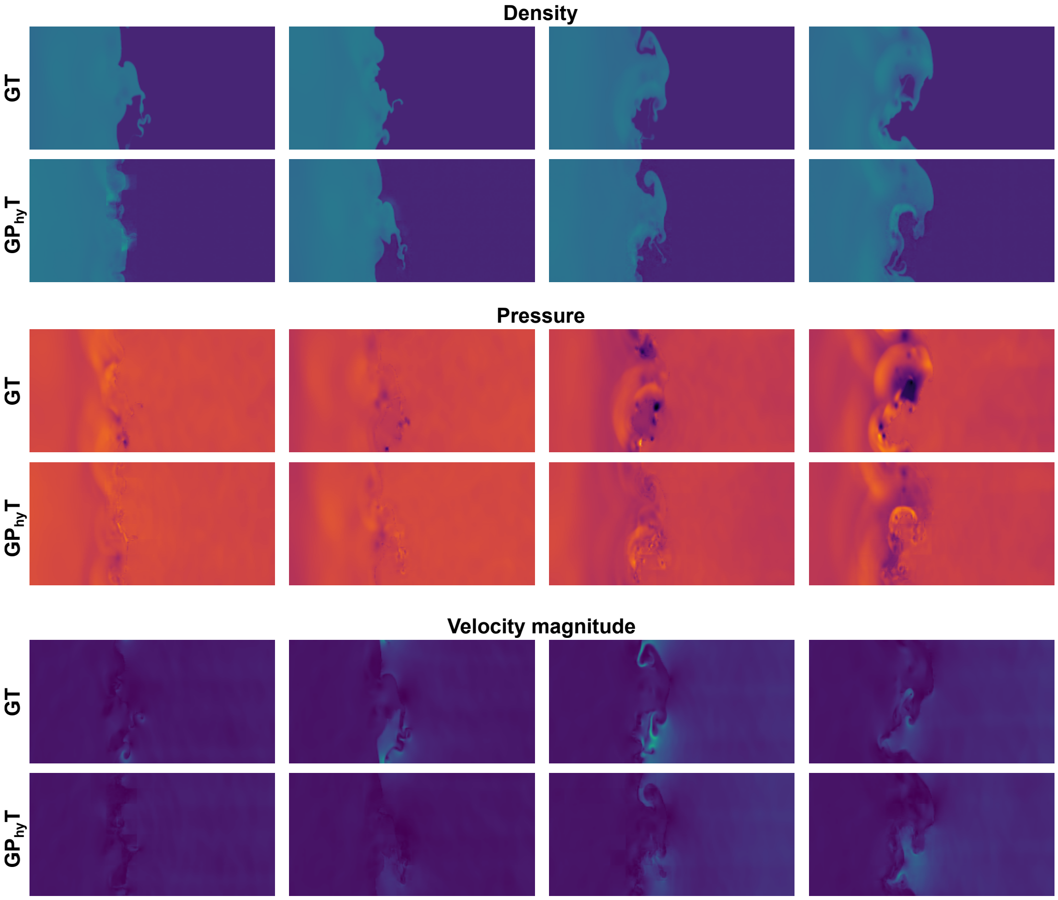

Figure 19: Next step predictions and ground truth (GT) for the novel turbulent radiative layer system for the fields density, pressure, and velocity magnitude (x and y combined), with a Δt of 1. Predictions are done by GP$_{\text{hy}}$T-XL.